

# An emerging pathway of Atlantic Water to the Barents Sea through the Svalbard Archipelago: drivers and variability

Kjersti Kalhagen<sup>1</sup>, Ragnheid Skogseth<sup>1</sup>, Till M. Baumann<sup>2,3</sup>, Eva Falck<sup>1</sup>, and Ilker Fer<sup>2,1</sup>

<sup>1</sup>Department of Arctic Geophysics, University Centre in Svalbard, Longyearbyen, Svalbard

<sup>2</sup>Geophysical Institute, University of Bergen, and Bjercknes Centre for Climate Research, Bergen, Norway

<sup>3</sup>Institute of Marine Research, Bergen, Norway

**Correspondence:** Kjersti Kalhagen (kjerstik@unis.no)

**Abstract.** The Barents Sea, an important component of the Arctic Ocean, is experiencing changes in ocean currents, stratification, sea-ice variability, and marine ecosystems. Inflowing Atlantic Water (AW) is a key driver of these changes. Although AW predominantly enters the Barents Sea via the Barents Sea Opening, other pathways remain relatively unexplored. Summer climatology fields of temperature in the last century compared to 2000–2019 indicate warming in the trough Storfjordrenna and the shallow banks Hopenbanken and Storfjordbanken in the Svalbard Archipelago, and shoaling of AW, extending further into the "channel" between the islands Edgeøya and Hopen. This region emerges as a pathway of AW into the northwestern Barents Sea. One year-long records from a mooring deployed between September 2018 and November 2019 at the saddle in this channel, show the flow of Atlantic-origin waters into the Arctic domain of the northwestern Barents Sea. The average current is directed eastward, into the Barents Sea, but shows a large variability throughout the year. Here, we investigate this variability on time scales from hours to months. Wind forcing mediates the currents and the water and heat exchange through the channel via geostrophic adjustment to Ekman transport. The main drivers for the warm inflow and the cross-saddle transport of positive temperature anomalies are persistent strong semidiurnal tidal currents, intermittent wind-forced events, and wintertime warm water intrusions forced by upstream conditions. We propose that similar topographic constraints where the Polar Front acts like a barrier may become more important in the future. The ongoing warming and shoaling of AW and changes in the large-scale weather patterns would likely increase the warm inflow and heat transport through the processes identified in this study.

## 1 Introduction

The shallow Barents Sea (Fig. 1) plays a crucial role in the Arctic climate system, serving as one of the two main gateways for Atlantic Water (AW) to enter the Arctic Ocean (e.g., Schauer et al., 2002; Smedsrud et al., 2013). Recent "Atlantification" in the Arctic Ocean (Årthun et al., 2012; Polyakov et al., 2017), characterised by ocean warming, weakening stratification, and declining winter sea ice (Shu et al., 2021), is partly fed by AW circulating through the Barents Sea (e.g., Asbjørnsen et al., 2020). The largest volume of AW enters the Barents Sea through the Barents Sea Opening (BSO, Fig. 1). In addition, AW can enter the northwestern Barents Sea through the Northern Barents Sea Opening (Lind and Ingvaldsen, 2012; Lundesgaard et al., 2022), from the branch that enters the Arctic Ocean through Fram Strait and flows north of Svalbard (e.g., Lind and Ingvaldsen, 2012). As AW flows through the Barents Sea, it is modified and transformed due to intense cooling through heat

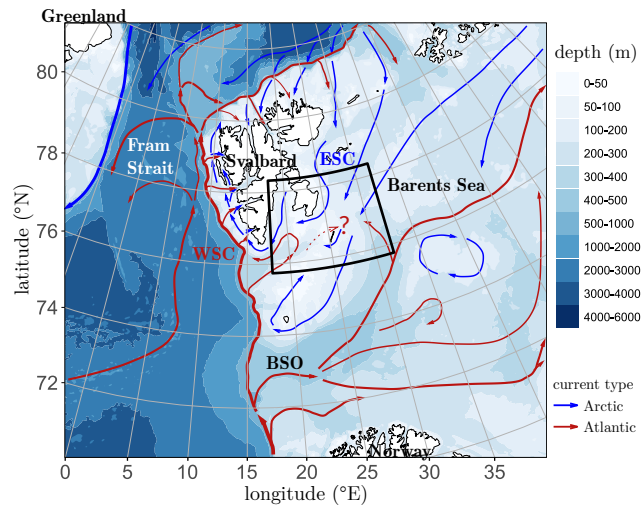


**Figure 1.** Bathymetry in the western Barents Sea and Fram Strait (IBCAO version 3, Jakobsson et al. (2012)) and general circulation (arrows, Vihtakari et al. (2019), adapted from Eriksen et al. (2018)). The West Spitsbergen Current (WSC), the East Spitsbergen Current (ESC) and the Barents Sea Opening (BSO) are marked. The black rectangle depicts the area shown in the detailed map in Fig. 2.

25 loss to the atmosphere (Häkkinen and Cavalieri, 1989; Årthun and Schrum, 2010; Lind et al., 2018; Ivanov et al., 2020), brine  
 release from sea-ice growth (e.g., Schauer et al., 2002; Ivanov et al., 2020), and mixing with the cooler and fresher Arctic  
 Water (Loeng, 1991; Lind et al., 2018) and denser brine-enriched waters (Schauer et al., 2002). The Barents Sea has been  
 termed a "cooling machine" (Smedsrud et al., 2013) whereby AW is transformed into Barents Sea Water. It is an important  
 area for dense water production (Knipowitsch, 1905; Midttun, 1985; Schauer et al., 2002; Årthun et al., 2011) and a source of  
 30 intermediate waters to the Arctic Ocean (Rudels et al., 1994; Schauer et al., 1997, 2002; Rudels et al., 2013).

Large-scale environmental changes have been observed in the Barents Sea over the past decades (Oziel et al., 2016; Skagseth  
 et al., 2020; Isaksen et al., 2022; Smedsrud et al., 2022). The loss of winter sea ice in the Arctic in recent times has been most  
 pronounced in the Barents Sea (Onarheim and Årthun, 2017; Rieke et al., 2023), which is the first Arctic sea projected to be  
 ice-free year-round (Årthun et al., 2021). Increased heat transport through the BSO is an important driver of the sea ice loss,  
 35 warming, and Atlantification in the Barents Sea (Årthun et al., 2012; Asbjørnsen et al., 2020). Increasing air temperatures also  
 drive sea ice loss. In the northern Barents Sea, the surface air temperatures have risen twice as fast as the Arctic as a whole  
 (Isaksen et al., 2022). Decreased import of sea ice into the northern Barents Sea is another factor in the increased sea ice loss  
 (Lind et al., 2018; Ingvaldsen et al., 2021), resulting in reduced freshwater input and a weakening of the stratification (Lind  
 et al., 2018). The weakening stratification facilitates enhanced vertical mixing and increased heat fluxes which may further  
 40 inhibit sea ice formation (Lind et al., 2018). Further hydrographic changes in the Barents Sea include increased salinity and a  
 diminishing presence of Arctic Water (Lind et al., 2018), changes in the Polar Front (Barton et al., 2018; Kolås et al., 2023),  
 which marks the boundary between waters of Atlantic and Arctic origins, and a poleward shift of the region where the cooling  
 machine is efficient (Skagseth et al., 2020; Shu et al., 2021).

The Atlantification of the Barents Sea has consequences for the ecosystem (Gerland et al., 2023), such as increased produc-  
45 tion, northward expansion of boreal species, reduction of the ice-associated ecosystem compartment, and increased connectivity  
in the food web (Ingvaldsen et al., 2021). The Barents Sea net primary production has increased substantially in the last two  
decades (Dalpadado et al., 2020; Lewis et al., 2020). Boreal zooplankton has expanded northwards (Geoffroy et al., 2018),  
while some Arctic zooplankton species have retreated (Eriksen et al., 2017). The northward expansion of Atlantic zooplankton  
species is anticipated to increase, with possible impacts on the Arctic zooplankton communities (Wold et al., 2023). Changes  
50 in biomass and distribution are also observed higher up in the food web (Gerland et al., 2023, and the references therein).

Although BSO is the main gateway of AW into the Barents Sea, other inflow zones such as the Northern Barents Sea Opening  
can be important. As the West Spitsbergen Current (WSC) transports AW northward towards Fram Strait, some AW is directed  
into the trough Storfjordrenna in the Svalbard Archipelago (Fig. 2), north of the BSO and the shallow bank Spitsbergenbanken.  
In Storfjordrenna, AW flows cyclonically, guided by topography, with shallow areas to its right (Schauer, 1995; Vivier et al.,  
55 2023).

Storfjordrenna has had a positive sea surface temperature (SST) trend from 1982 to 2020 and the largest SST increase in the  
Barents Sea during the period from 1995 to 2007 (Bayoumy et al., 2022b), due to the increased inflow of AW following shall-  
lower isobaths than earlier. Following a year of record-low sea ice cover, the surface layers in Storfjorden and Storfjordrenna  
were replaced by warmer and more saline Arctic Water during summer 2016 (Vivier et al., 2023). Summer of 2016 had the  
60 warmest and longest-lasting marine heatwave in the Barents Sea so far (Bayoumy et al., 2022a).

Northeast of Storfjordrenna, on the Arctic side of the Polar Front, lies the Olga Basin (Fig. 2). Here, the Arctic Water  
layer is the coldest and thickest compared to the rest of the northern Barents Sea (Lind and Ingvaldsen, 2012). Arctic Water  
enters through the gaps and troughs in the northern Barents Sea (Dickson et al., 1970; Loeng, 1991) and circulates with the  
East Spitsbergen Current (Quadfasel et al., 1988; Loeng, 1991). In addition to Arctic Water, AW enters the Olga Basin at  
65 depth through the gateways in the north (Lind and Ingvaldsen, 2012; Lundesgaard et al., 2022) and to a smaller degree over  
the  $\approx 200$  m deep saddle separating the Olga Basin from the trench Hopen djupet to the south (Kolås et al., 2023; Lind and  
Ingvaldsen, 2012) (Fig. 2).

The channel between Edgeøya and Hopen islands (Fig. 2) separates the increasingly warm and shoaling AW in Storfjor-  
drenna from the Olga Basin, the Arctic domain in the northwestern Barents Sea. Here, we investigate the physical processes  
70 that drive and mediate the inflow of Atlantic-origin water masses into the Olga Basin. Such warm water inflow can potentially  
reduce growth, accelerate sea ice melt and change the deep basin stratification in the Olga Basin. The (increasing) presence of  
warm Atlantic-origin waters in Storfjordrenna may also have implications for the properties of the East Spitsbergen Current  
crossing the channel westward, Storfjorden, and the coastal environment west of Spitsbergen. We propose that the study site  
may be an increasingly relevant pathway for warm waters into the Arctic domain of the Barents Sea. Using novel data from  
75 a less-explored region, we identify and discuss the variability of the currents and heat exchange on time scales from hours to  
months.

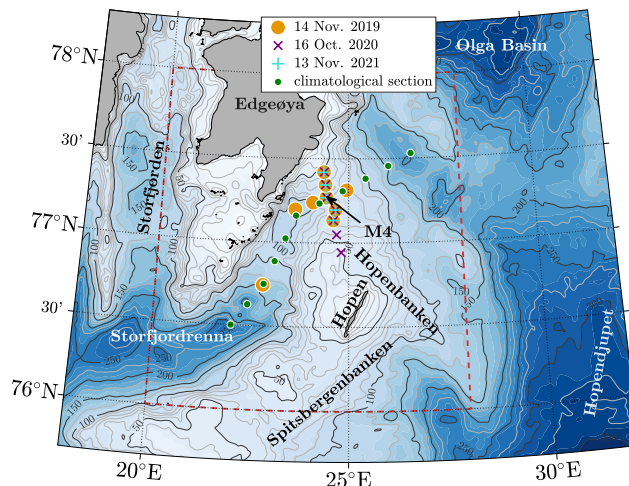


**Figure 2.** Bathymetry in the mooring area (IBCAO version 4, Jakobsson et al. (2020)). The mooring M4 (black arrow) is located on the saddle on Hopenbanken between the trough Storfjordrenna and the interior of the northwestern Barents Sea. The saddle is bounded to the north and south by the islands Edgeøya and Hopen, respectively. Hydrographic stations from 14 November 2019, 16 October 2020, and 13 November 2021 and the climatological section in Fig. 4 are marked (see legend). The dashed red rectangle shows the span of Fig. 3.

## 2 Data and Methods

### 2.1 Data

In this study, we use a combination of historical hydrographic data, recent hydrographic transects during late autumn, and a year-long hydrographic and current time series from a mooring. The mooring was deployed at 70 meter depth on the shallow bank Hopenbanken, between the trough Storfjordrenna and the interior of the Barents Sea (Fig. 2).

The historical data include hydrographic profiles extracted from UNIS Hydrographic Dataset (UNIS HD; Skogseth et al. (2019)) covering the vicinity of the mooring area over the period 1930–2019.

The recent hydrographic transects were collected on 14 November 2019 onboard *Kronprins Haakon* (Sundfjord and Renner, 2021), on 16 October 2020 onboard *G. O. Sars* (Fer et al., 2021), and on 13 November 2021 onboard *Kronprins Haakon* (Renner and Sundfjord, 2022).

Temperature, salinity, and ocean currents were measured using instruments on the mooring from 29 September 2018 to 14 November 2019, located at  $77^{\circ} 16.116' N$ ,  $24^{\circ} 24.402' E$  (Fig. 2). The mooring was a trawl-proof bottom frame and consisted of one conductivity-temperature-depth recorder (CTD, an unpumped Seabird Microcat SBE37-SM) and one Acoustic Doppler current profiler (ADCP, a Nortek Signature 250) placed inside the frame with transducers pointing upward. The Microcat recorded temperature, salinity, and pressure near the bottom at about 68 m, for the whole period at a sampling interval of 15 min. The ADCP profiled current speed and direction through the water column with 25 cells of 3 m thickness at an averaging interval of 20 min. All data from the mooring were interpolated onto a common hourly time vector before analysis.

We corrected the velocity direction for magnetic declination of  $15^\circ$ . The ADCP compass was further checked by comparing the tidal ellipses obtained from the observed current velocity with those from the Arctic Ocean 5 km Inverse Model 2018 (Arc5km2018) (Erofeeva and Egbert, 2020). For the  $M_2$  constituent, the ellipse inclinations from the Arc5km2018 and the depth-average measured current were approximately the same. For the other significant semidiurnal constituents  $S_2$ ,  $N_2$ ,  $K_2$ , the ellipse properties from the measured currents were in fairly good agreement with Arc5km2018, i.e., ellipse inclinations agreed within  $14^\circ$  and semimajor axes within  $1 \text{ cm s}^{-1}$ . Since  $M_2$  is the dominant constituent in the study area, no further compass corrections were found necessary. We then referenced the current velocity profiles to the surface to account for sea level variations that were detected by the altimeter of the ADCP.

We extracted wind speed and direction in the region from the ERA5 reanalyses (hourly data on single levels, with a spatial resolution of  $0.25^\circ$ , Hersbach et al. (2020)), and sea surface temperature (SST) and sea ice concentration (SIC) from the Global Ocean OSTIA Sea Surface Temperature and Sea Ice Reprocessed product (daily data with a spatial resolution of  $0.05^\circ$ , OSTIA (2023); Good et al. (2020)).

All data used in the study are openly available as detailed in the data availability section.

## 2.2 Data analysis methods

The historical hydrographic data (Skogseth et al., 2019) have been optimally interpolated onto horizontal and vertical climatological sections to compare the two recent decades (2000–2019) to the previous century (1930–2000). Due to temporally and spatially sparse data coverage, only summer (July–October mean) sections were created. A description of gridding and interpolation is given in Appendix A, together with data coverage and standard deviations for the climatological maps and vertical sections.

Temperature and practical salinity from the recent hydrographic transects, from the mooring, and the optimally interpolated climatological sections were converted to Conservative Temperature and Absolute Salinity following TEOS10 (McDougall and Krzysik, 2015). In the following, we use the subscript  $b$  (for bottom) to refer to temperature  $T_b$  and salinity  $S_b$  near the seafloor. AW is defined as water with Conservative Temperature  $\Theta \geq 2^\circ\text{C}$  and Absolute Salinity  $S_A \geq 35.06 \text{ g kg}^{-1}$  (Sundfjord et al., 2020). We refer to the Atlantic-origin water as the AW that is modified or transformed en route from the WSC through Storfjordrenna into relatively warm and saline water compared to the surrounding water masses, but colder and less saline than pure AW. This inflow of warm water into the Barents Sea affects the deep basin stratification, and the sea ice growth and melt.

We identify the time scales of variability using spectral analysis. Cartesian and rotary spectral components were estimated following the multitaper method from Percival and Walden (1993) with Slepian data tapers (e.g., Slepian, 1978; Thomson, 1982). To analyse the time-variability of the spectral components, wavelet transforms following Lilly and Olhede (2009) with generalised Morse wavelets (Olhede and Walden, 2002) were used. The values for the parameters that define the Morse wavelets were chosen to be  $\gamma = 3$  for symmetric wavelets and  $\beta = 5$  to resolve the variability on time scales between semidiurnal and a few weeks in both frequency and time.

The spectral analysis revealed three frequency bands with dominant variability, which we associate with semidiurnal tides (periods of ten hours to 14 hours), "weather-band" processes (28 hours to 10 days), and lower-frequency activity (seven days

to six weeks). To study these fluctuations, we filtered the time series with a Butterworth band-pass filter with an order as high as possible while ensuring stability for each frequency band, order 5 for semidiurnal tides and weather-band, and order 3 for  
130 lower-frequency activity.

To describe and visualise the background conditions in hydrography and currents, we used a low-pass Butterworth filter of order 6 and a cutoff frequency corresponding to 10 days.

We analyse the current velocity data from the mooring to study the mean flow properties and variability of the flow in time scales associated with tidal variability, weather-band processes, and lower-frequency events. For this we used two different  
135 coordinate system rotations. The coordinate system was rotated with  $-42^\circ$  to align with the long-term mean flow along the isobaths. The rotated velocity components are denoted as  $u_R$  and  $v_R$  for the along- (roughly southeast) and across-isobath (roughly northeast) directions. In the analysis of variability at selected time scales, we apply another rotation of the velocity components denoted as  $u_r$  and  $v_r$ . These are the components along and across the direction of the highest variance in the frequency bands associated with weather and lower-frequency activity. This coordinate system is rotated with  $-28^\circ$  so that  $u_r$ ,  
140 is directed roughly toward east-southeast and  $v_r$  toward north-northeast.

Eddy temperature fluxes were calculated as  $\overline{u_r' T'}$  and  $\overline{v_r' T'}$ , where  $T'$  denotes fluctuations of the near-bottom temperature, and  $u_r'$  and  $v_r'$  are the velocity component fluctuations along ( $-28^\circ$  off east) and across ( $+62^\circ$  off east) the direction of highest variance in the frequency bands associated with weather and lower-frequency activity. The fluctuations (denoted by primes) were obtained by band-pass filtering the time series. The velocity data are layer-averaged over the bottom half of the water  
145 column. While the water column is at times stratified in temperature, available CTD profiles suggest that the lower half of the water column is typically well mixed thus temperature measured close to the bottom may be regarded to be representative for the lower half of the water column. The overline denotes a 30-day moving average.

Wind stress was calculated as  $(\tau_x, \tau_y) = \rho_{\text{air}} C_D |\mathbf{u}_{10\text{m}}| (u_{10\text{m}}, v_{10\text{m}})$ , where  $\rho_{\text{air}} = 1.25 \text{ kg m}^{-3}$  is the density of air,  $\mathbf{u}_{10\text{m}} = (u_{10\text{m}}, v_{10\text{m}})$  is the wind vector with the eastward and northward components of wind velocity at 10 m from ERA5,  $|\mathbf{u}_{10\text{m}}|$  is its magnitude, and  $C_D$  is the drag coefficient. We used  $C_D$  dependent on the sea ice concentration following Lüpkes and Birnbaum (2005). Ekman transport is calculated from the wind stress using  $(U_E, V_E) = \frac{1}{\rho_0 f} (\tau_x, -\tau_y)$ , where  $\rho_0 = 1027 \text{ kg m}^{-3}$  is the reference density of sea water and  $f$  is the Coriolis parameter.  
150

Time series of SST, SIC, wind velocity, and wind stress at the mooring location, were obtained by spatially interpolating onto the mooring location from the original grids, i.e. from  $0.05^\circ$  for SST and SIC and  $0.25^\circ$  for wind velocity.

## 155 3 Results

### 3.1 Long-term changes in the hydrographic environment in Storfjordrenna and on Hopenbanken

The hydrographic environment in the trough Storfjordrenna and the shallow banks Hopenbanken and Storfjordbanken (Fig. 2) has undergone warming over the past two decades. Summer climatology maps of the depth-averaged temperature in 1930–2000 (Fig. 3a) and in 2000–2019 (Fig. 3b) indicate warming over most of the area. Observed increase in average temperature exceeds

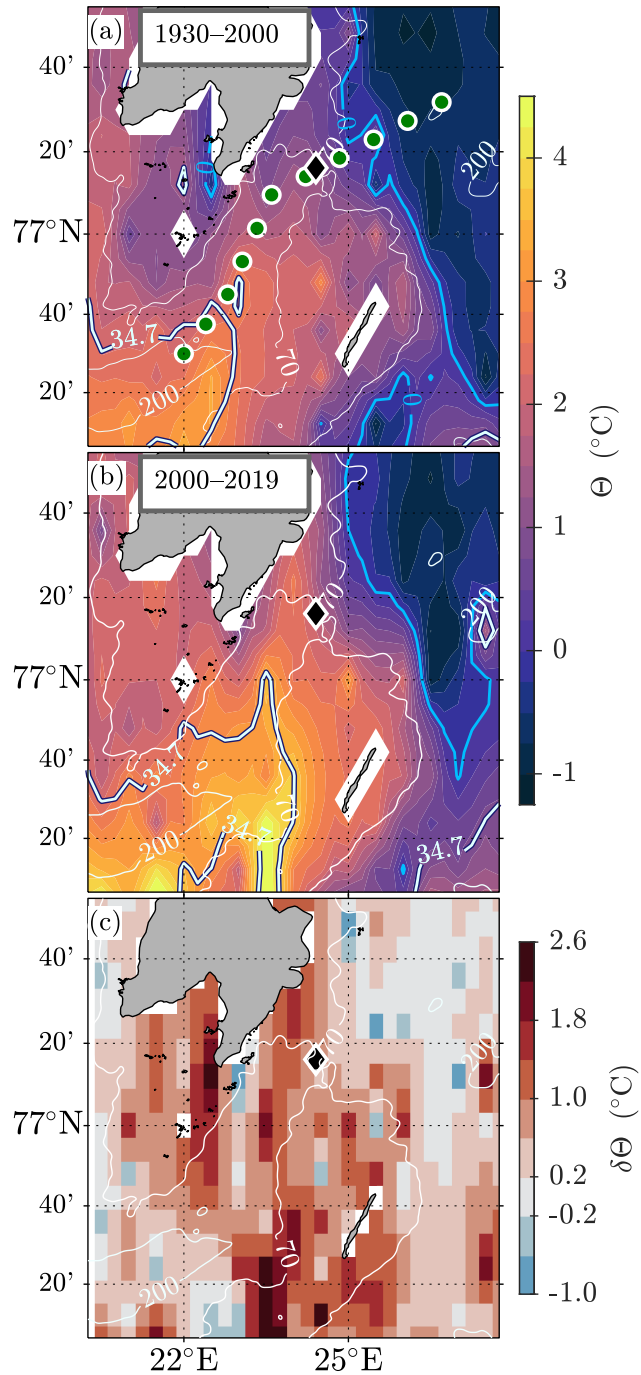


**Figure 3.** Climatological maps of depth-averaged Conservative Temperature  $\Theta$  ( $^{\circ}\text{C}$ ) for a) 1930–2000, b) 2000–2019, and c) their difference (1930–2000 subtracted from 2000–2019). In (a–b) the  $0^{\circ}\text{C}$  isotherm (blue) and the  $34.7 \text{ g kg}^{-1}$  isohaline (contrasted pale blue) are shown for reference. In a), the vertical section in Fig. 4 is shown as green dots and the mooring position as a black diamond. The 70 m and 200 m isobaths are indicated with white contours.

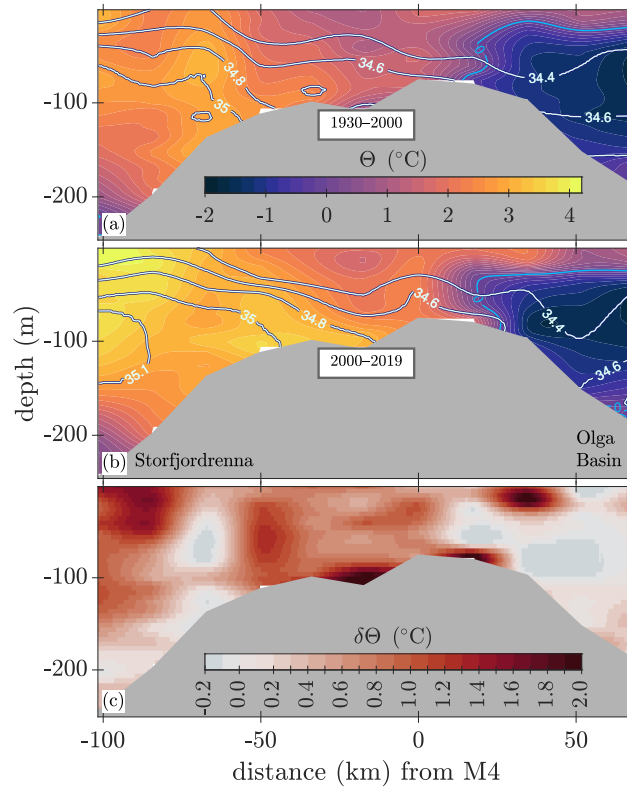


**Figure 4.** Climatological vertical hydrographic sections from Storfjordrenna, across the saddle, and into the Olga Basin for a) 1930–2000, b) 2000–2019, and c) difference (1930–2000 subtracted from 2000–2019). a–b) Conservative Temperature  $\Theta$  ( $^{\circ}\text{C}$ ) in colours and the  $0^{\circ}\text{C}$  isothermal highlighted in blue. The  $34.4\text{ g kg}^{-1}$ ,  $34.6\text{ g kg}^{-1}$ ,  $34.8\text{ g kg}^{-1}$ ,  $35.0\text{ g kg}^{-1}$ , and  $35.1\text{ g kg}^{-1}$  isohalines are shown as contrasted pale blue curves. c) Difference of Conservative Temperature  $\delta\Theta$  ( $^{\circ}\text{C}$ ) in colours. Horizontal axis shows the distance to the mooring position, with positive values towards the Olga Basin. The location of the section is indicated with green dots in Fig. 3a.

160  $1^{\circ}\text{C}$  over large parts of Hopenbanken and Storfjordbanken (Fig. 3c). The warming is observed both at the surface and at depth (not shown). The  $34.7\text{ g kg}^{-1}$  isohaline has extended further northeast in 2000–2019 relative to 1930–2000 (Fig. 3a–b).

The vertical climatological section from Storfjordrenna, across the saddle on Hopenbanken, and into the Olga Basin (Fig. 4) shows that waters of Atlantic origin have shoaled in the water column and now reach further east towards the saddle. The warming has occurred through the water column and the saddle area has warmed by  $1^{\circ}\text{C}$  to  $2^{\circ}\text{C}$ . Additionally, salinity has  
 165 increased by  $0.05\text{ g kg}^{-1}$  to  $0.35\text{ g kg}^{-1}$  over intermediate depths in Storfjordrenna (not shown). We also note that the recent two decades show a deepening of the  $34.4\text{ g kg}^{-1}$  isobath and a co-located decrease in temperature toward the Olga Basin (Fig. 4b–c).



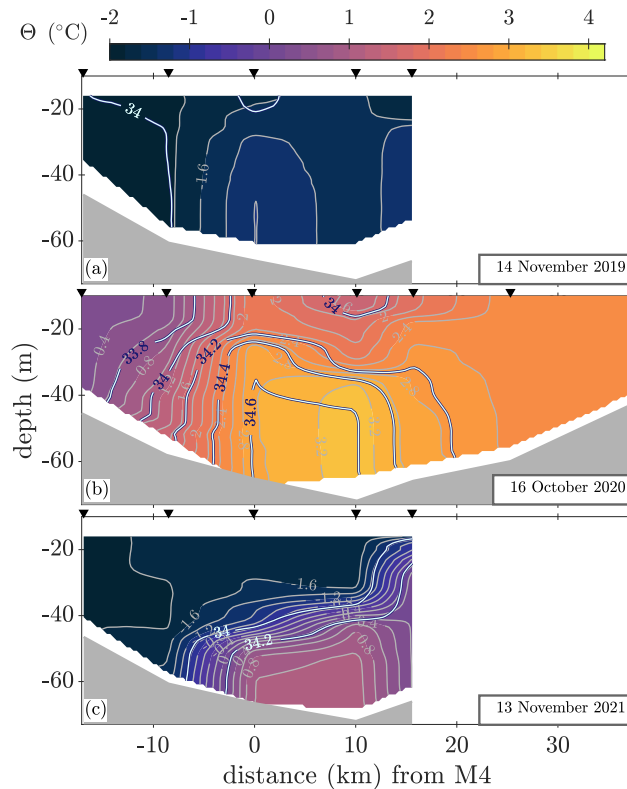


**Figure 5.** Hydrographic transects along the saddle between Storfjordrenna and the Barents Sea in a) 14 November 2019, b) 16 October 2020, and c) 13 November 2021 with Conservative Temperature in colour (contours every  $0.2\text{ }^{\circ}\text{C}$  and Absolute Salinity in contrasted pale blue contours (every  $0.2\text{ g kg}^{-1}$ ). The northern part of the saddle (close to Edgeøya) is to the left, and the southern part (towards Hopen) is to the right. The horizontal axis shows the distance to the mooring position M4, with positive values towards the south.

### 3.2 Late-autumn hydrographic transects indicate large variability

Recent hydrographic transects covering the saddle region collected in November 2019, October 2020, and November 2021 (Fig. 5) show that the mooring is in an area with thermal and haline gradients, with local temperature and salinity maxima near the mooring position in late autumn.

In November 2019, the transect along the saddle was cold and relatively fresh but had remnants of heat (Fig. 5a). The warmest water of  $-1.2\text{ }^{\circ}\text{C}$  was found at the mooring position in the lower half of the water column. In the northern side of the transect, the temperature was near the freezing point with relatively high salinity (Fig. 5a). At this time, AW was present in Storfjordrenna and close to the mooring (not shown): 70 km southwest of the mooring, water at  $2.9\text{ }^{\circ}\text{C}$  to  $3.7\text{ }^{\circ}\text{C}$  and  $34.84\text{ g kg}^{-1}$  to  $35.02\text{ g kg}^{-1}$  was found at depth, which is within the temperature range for pure AW and slightly lower than the salinity threshold of  $35.06\text{ g kg}^{-1}$  (Sundfjord et al., 2020). Also relatively warm water of around  $0.5\text{ }^{\circ}\text{C}$  was situated at depth 10 km to the west of the mooring position.

In October 2020, warm and saline water of Atlantic origin occupied the lower half of the water column (Fig. 5b). The warmest water at  $3.3^{\circ}\text{C}$  and a salinity of  $34.6\text{ g kg}^{-1}$  was located 10 km south of the mooring position. Water warmer than  $2^{\circ}\text{C}$  reached the surface at the mooring position and between 15 km and 37 km south of the mooring position. The coolest and least saline water was found on the northern side of the transect. At a station 60 km to the northeast, we observed water at  $1^{\circ}\text{C}$  and salinity  $35.0\text{ g kg}^{-1}$  below 150 m depth (not shown).

In November 2021, the temperature maximum of  $1^{\circ}\text{C}$  at and south of the mooring position (Fig. 5c) was warmer than that in November 2019 (Fig. 5a). The isohalines were also aligned with the isotherms with salinities exceeding  $34.2\text{ g kg}^{-1}$  for the water at  $\geq 0^{\circ}\text{C}$  at depth on the southern side. The northern side of the transect was below  $-1.75^{\circ}\text{C}$  as it was in November 2019.

### 3.3 Seasonal variability in hydrography and current velocity from mooring records

Early in the record, both the near-bottom temperature,  $T_b$ , and salinity,  $S_b$ , increased to values close to the pure AW properties by the middle of October (Fig. 6c). Temperature near the bottom was higher than the SST, and the increase in  $T_b$  and  $S_b$  coincided with a relatively strong and long-lasting surface-intensified current directed southeast along-isobath ( $u_R$ , Fig. 6d). Following the maxima in near-bottom temperature and salinity, the water column gradually cooled until mid-January 2019, when both  $T_b$  and SST nearly reached the freezing point (Fig. 6c). During these months,  $u_R$  oscillated between  $-5\text{ cm s}^{-1}$  and  $10\text{ cm s}^{-1}$  at a two-week time scale with a negligible depth variability over the measured range (Fig. 6d). Temperature and salinity co-varied with  $u_R$ , with  $T_b$  and  $S_b$  lagging  $u_R$  by 3.3 days and 4.8 days, respectively. Sea ice was first observed over the saddle in late December (Fig. 6b).

From mid-January to mid-June 2019, there was a partial sea ice cover over the saddle (Fig. 6b),  $T_b$  and SST were generally at or close to the freezing point (Fig. 6c).  $S_b$  increased, probably as a result of brine release from sea ice formation, reaching its highest value  $35.12\text{ g kg}^{-1}$  by the end of March, gradually decreasing thereafter (Fig. 6c). The current was more unidirectional than during autumn, i.e.  $u_R$  was generally positive (Fig. 6d) and varied typically between  $5\text{ cm s}^{-1}$  and  $10\text{ cm s}^{-1}$ , episodically exceeding  $20\text{ cm s}^{-1}$ .

Although the saddle was ice-covered and the water was generally near the freezing point during winter and spring, there were several episodes when  $T_b$  and SST increased, coinciding with a reduction of the SIC and an enhancement of  $u_R$  (Fig. 6b–d). The first and largest increase in  $T_b$  and SST occurred in early February 2019 after a sharp reduction of SIC at the end of January when the sea ice cover that had built up over two weeks during northerly winds disappeared in two days. The wind direction changed to southerly and  $u_R$  changed to positive values shortly before the sea ice disappeared from the saddle (Fig. 6a and d). The surface-intensified  $u_R$  increased in strength during and after the sea ice disappeared and reached a maximum of  $26\text{ cm s}^{-1}$  close to the surface (Fig. 6d).  $T_b$  and SST increased to  $0.9^{\circ}\text{C}$  and  $0.4^{\circ}\text{C}$ , respectively, shortly after and remained above the freezing point for more than a month (Fig. 6c). During this time, the wind direction turned and stayed northerly and the partial sea ice cover was reestablished over the saddle (Fig. 6a–b).  $T_b$  and SST, however, remained above the freezing point and reached smaller maxima, and  $u_R$  further increased in strength, reaching  $34\text{ cm s}^{-1}$  at the beginning of March, the highest value measured during the whole sampling period (Fig. 6c–d).

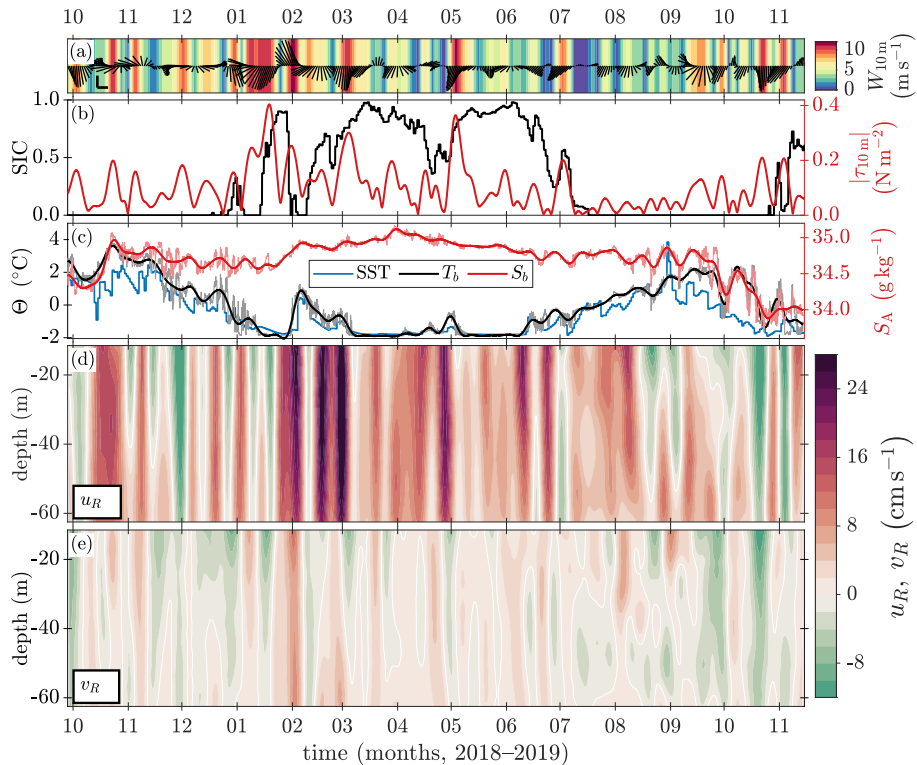


**Figure 6.** Time series over the mooring deployment period (29 September 2018 to 14 November 2019) of a) wind speed (colours) and wind velocity (quivers every 24 hours, an upward pointing vector is wind blowing northward, reference quivers are  $5 \text{ cm s}^{-1}$ ), b) sea ice concentration (SIC) (black, left axis) and wind stress  $\tau_{10m}$  ( $\text{N m}^{-2}$ ) (red, right axis), c) Conservative Temperature  $\Theta$  ( $^{\circ}\text{C}$ ) near the bottom (black), sea surface temperature (SST,  $^{\circ}\text{C}$ ) (blue), and Absolute Salinity  $S_A$  ( $\text{g kg}^{-1}$ ) near the bottom (red, right axis), d) along-isobath ( $-42^{\circ}$ , directed southeastward) velocity component,  $u_R$ , and e) cross-isobath ( $+48^{\circ}$ , northeastward) velocity component,  $v_R$ . Wind velocity, wind stress, mooring temperature and salinity, and current velocity are low-pass filtered with a cutoff-frequency corresponding to 10 days.  $\Theta$  ( $^{\circ}\text{C}$ ) and  $S_A$  ( $\text{g kg}^{-1}$ ) are shown as both unfiltered (pale, thin curves) and low-pass filtered (dark, thick curves). SST and SIC are daily values. Wind velocity, SST, and SIC were interpolated spatially onto the mooring position.

The SIC started to decrease in June and the area was ice-free from mid-July (Fig. 6b). Most of the reduction of the sea ice cover occurred during two pulses of increased  $u_R$  in the second half of June which preceded two pulses of increased  $T_b$  and SST (Fig. 6d, c). After the sea ice cover had disappeared,  $u_R$  became weaker, less unidirectional, and occasionally more depth-variable (Fig. 6d). From July through August, the water column steadily warmed. From September until the end of the measurement period in mid-November 2019, SST decreased toward the freezing point while  $T_b$  was generally higher than SST.  $S_b$  generally co-varied with  $T_b$  during this autumn and overall decreased (Fig. 6c). By late October 2019, some sea ice had already drifted over the saddle and SST reached the freezing point, while  $T_b$  remained above the freezing point until the

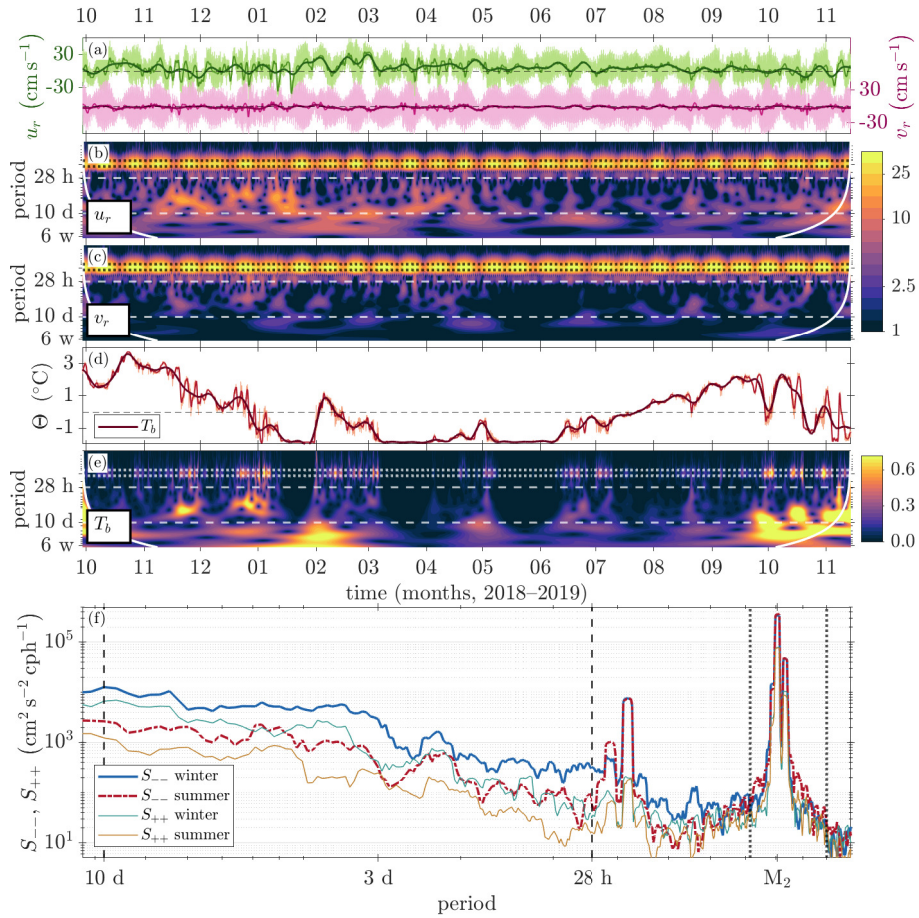


**Figure 7.** a) Time series over the mooring deployment period (29 September 2018 to 14 November 2019) of depth-averaged velocity component along  $-28^{\circ}$ ,  $u_r$  (green, left axis) and along  $+62^{\circ}$ ,  $v_r$  (pink, right axis), as measured (pale, thin curves), 28 hour low-pass filtered (darker, thicker curves), and 10 day-low-pass filtered (darkest, thickest curves). b–c) Wavelet transform of  $u_r$  (b) and  $v_r$  (c) in logarithmic scale. d) Time series of near-bottom temperature  $T_b$  with the same filtering as in (a). e) Wavelet transform of  $T_b$  in linear scale. f) Rotary spectra (anticyclonic: thick curves; cyclonic: thin curves) of the depth-averaged current velocity for winter (October to March, blue and green curves) and summer (April to September, red and yellow curves). White curves in (b,c,e) show the area affected by edge effects. The cutoff frequencies for the semidiurnal tidal band (dotted lines) and the weather band (dashed lines) are shown as horizontal lines in (b,c,e) and vertical lines in (f).

220 mooring was recovered in mid-November (Fig. 6b, c). Compared to the previous autumn, in autumn 2019, the near-bottom waters were both colder and less saline, and sea ice was established earlier.

### 3.4 Mesoscale and tidal variability

Wavelet analysis of current components  $u_r$  and  $v_r$  (along  $-28^\circ$  and  $+62^\circ$ , respectively) reveals year-round dominance of semidiurnal tidal currents with a clear spring–neap cycle (Fig. 7a–c). The semidiurnal tidal current was anticyclonic (Fig. 7f) with variance oriented along  $+25^\circ$ , i.e., near east-northeast (Section 3.6). When the near-bottom temperature  $T_b$  was above the freezing point, its semidiurnal variability was typically within  $0.2^\circ\text{C}$  to  $0.6^\circ\text{C}$ , but occasionally reaching  $0.8^\circ\text{C}$ .

Weather-band variability (28 hours to 10 days) was considerable, particularly during the autumn months (November 2018 into January 2019) (Fig. 7b, c, e), with the principal axis along the WNW–ESE direction, approximately aligned with topography, Section 3.6).  $T_b$  anomalies were typically within  $\pm 0.5^\circ\text{C}$ , but doubled in November–December 2018 and October–November 2019. In the beginning (October 2018) and toward the end of the record (October–November 2019),  $T_b$  has elevated variance at the time scale of 10 days; however, the edge effects of the wavelet analysis are significant (Fig. 7e).

The anticyclonic velocity component was generally more energetic than its cyclonic counterpart (Fig. 7f). The semidiurnal current had almost ten times more variance in the anticyclonic component, and the diurnal band had almost all variance in the anticyclonic component. At lower frequencies, the currents were anticyclonic and elliptically polarized year-round (Fig. 7f), except in winter when the currents became nearly linearly polarized at periods of two or more weeks (not shown).

### 3.5 Impact of wind forcing on the across-saddle current

The strength and direction of the overflow current are influenced by large-scale winds (Fig. 8). Regression analysis shows that the depth-averaged current anomalies along  $-28^\circ$  in the frequency band from 28 hours to 10 days ( $u_r'$ ) depend on the Ekman transport along the same axis. Geostrophic adjustment to Ekman transport during north-northeasterly winds typically opposes the east-southeastward cross-saddle current (Fig. 8c), and in the case of anomalously strong winds, even reverses it (Fig. 8b). Conversely, weaker and/or southerly winds tend to enhance the eastward flow into the Barents Sea (Fig. 8d).

Anomalously strong north-northeasterly winds, causing Ekman transport values below the 10th percentile ( $U_{E_r} = -1.84(\pm 0.53) \text{ m}^2 \text{ s}^{-1}$  for daily averages), are associated with the strongest current reversal events ( $u_r' = -5.1(\pm 8.8) \text{ cm s}^{-1}$  for daily averages, with current flowing towards the WNW along topography) (Fig. 8b). The mean current velocity is then  $3.1 \text{ cm s}^{-1}$ , directed west-southwestwards, but with a large spread.

On the other hand, winds with a southerly component, causing Ekman transport values above the 90th percentile ( $U_{E_r} = 0.79(\pm 0.35) \text{ m}^2 \text{ s}^{-1}$  for daily averages), are associated with the strongest east-southeastward current events ( $u_r' = 4.4(\pm 6.3) \text{ cm s}^{-1}$  for daily averages) (Fig. 8d). This suggests that the normal east-southeastward current is accelerated by geostrophic adjustment to Ekman transport set up by winds with a southerly component. The average mean current in this case is  $14.1 \text{ cm s}^{-1}$  towards the east-southeast.

### 3.6 Eastward transport of positive temperature anomalies

Near-bottom temperature variability occurs in the same frequency bands as the current variability (Fig. 7). We separated the contributions from tides, weather-band processes, and lower-frequency mesoscale activity by band-pass filtering the time

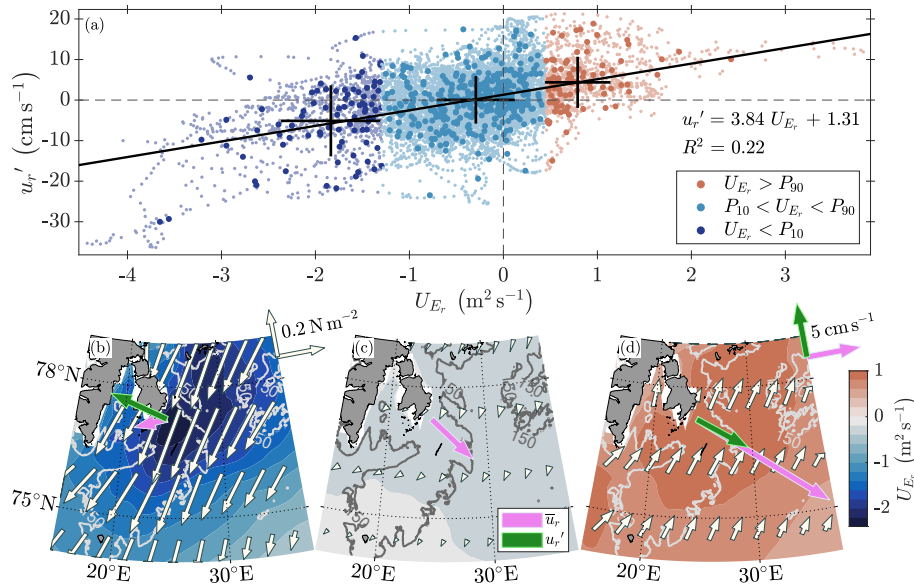


**Figure 8.** a) Ekman transport  $U_{E_r}$  ( $\text{m}^2 \text{s}^{-1}$ ) along  $-28^\circ$  versus the weather-band (28 h – 10 d) depth-averaged current speed anomalies along  $-28^\circ$   $u_r'$ . Colours indicate the  $U_{E_r}$  composites: below its 10th percentile (dark blue), corresponding to strong north-northeasterly winds, within its 10th and 90th percentiles (light blue), corresponding to weak north-northeasterly winds, and above its 90th percentile (orange), corresponding to modest south-southwesterly winds. The small, pale dots are hourly values, while the larger dots are daily averages. The current is lagged by 7 hours relative to the wind before calculating  $U_{E_r}$  and averaging in time. The error bars show the mean and standard deviations of the daily averages within each composite. Maps of composite averages of  $U_{E_r}$  (colour shading), wind stress (white quivers), mean current  $\bar{u}_r$  (pink quivers), and current anomalies  $u_r'$  (green quivers) for Ekman transport b) below its 10th percentile, c) within its 10th and 90th percentiles, and d) above its 90th percentile. Reference quivers for wind stress ( $0.2 \text{ N m}^{-2}$ ) and for current ( $5 \text{ cm s}^{-1}$ ) are shown in panels (b) and (d), respectively.

series of temperature and current velocity (Sect. 2.2). By analysing temperature anomalies  $T'$  in the velocity anomaly space  
 255  $(u', v')$ , we find that positive temperature anomalies were generally located in the southeast sector of the velocity anomalies, while negative temperature anomalies are in the northwest sector, resulting in net temperature transport across the saddle in the identified bands of variability (Fig. 9a–9c). This indicates a net heat transport southeastwards across the saddle. For the weather- and mesoscale frequency bands (Fig. 9b and Fig. 9c, respectively), the largest temperature anomalies were aligned with the principal axis of variability ( $-28^\circ$ ). In the semidiurnal (Fig. 9a) and diurnal tidal bands (not shown), however, the  
 260 largest temperature anomalies lied nearly perpendicular to the axis of maximum variance (major axes of the ellipses).

The eddy temperature flux  $\overline{u_r' T'}$  along the principal axis  $-28^\circ$  (Fig. 9d–f, solid curves) was generally positive through the year, with values typically between  $1 \text{ K cm s}^{-1}$  and  $2 \text{ K cm s}^{-1}$ . The largest semidiurnal tidal contribution occurred October–December in both years, with values on the order of  $1 \text{ K cm s}^{-1}$  directed towards the southeast. Comparable fluxes were also observed between February and July when warm and saline water intermittently appeared near the saddle. In the weather band,  
 265 the flux was large from November 2018 to January 2019 with values between  $1 \text{ K cm s}^{-1}$  and  $3 \text{ K cm s}^{-1}$ , and again during

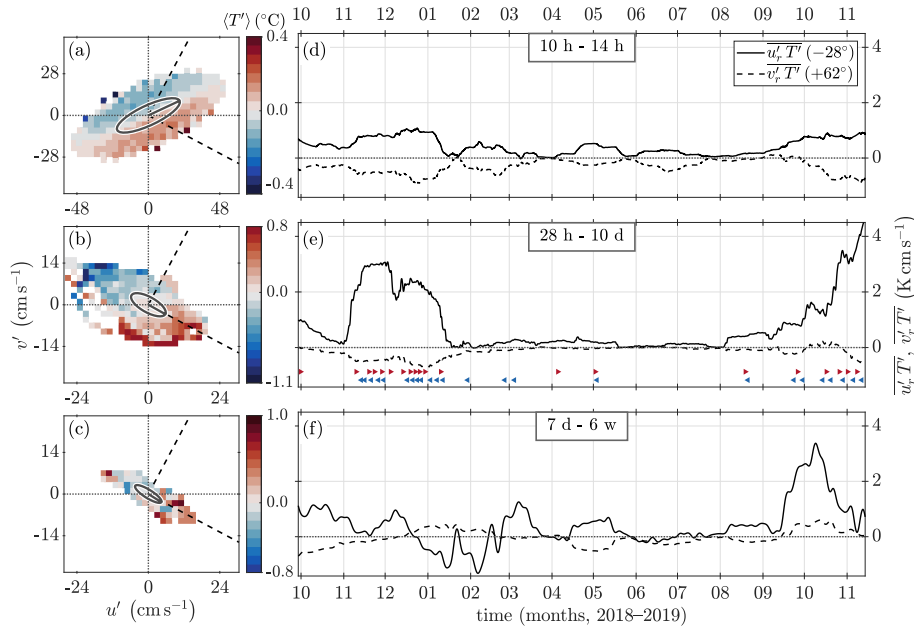


**Figure 9.** a, b, c) Temperature anomaly (colours) averaged in bins of current velocity anomalies analysed in the semidiurnal tidal band (a, d), weather band (28 hours to 10 days; b, e), and lower-frequency band (seven days to six weeks; c, f). The velocity anomalies are layer-averaged over the bottom half of the water column, and their variance ellipses are overlaid. d, e, f) Time series of eddy temperature flux along  $\overline{u_r' T'}$  ( $-28^\circ$ , solid curves) and across  $\overline{v_r' T'}$  ( $+62^\circ$ , dashed curves) the principal axis of the weather- and lower-frequency band variability shown in (b) and (c). The rotated coordinate system is indicated with dashed lines in the left column. Temporal averaging is done by running mean over 30 days. Note that the  $u'$  and  $v'$  ranges for the semidiurnal band are twice as high as for the other bands. In (e), the times of peaks chosen for ensemble averaging are marked with red triangles pointing right for positive temperature and along-isobath current anomalies, and blue triangles pointing left for negative anomalies.

autumn 2019, reaching  $5 \text{ K cm s}^{-1}$  by the end of the measurement period (Fig. 9e). Between mid-January and August 2019, the flux is negligible. Lower-frequency oscillations on timescales between one and six weeks exhibit sporadic episodes of large positive eddy temperature flux values during autumn and winter, reaching  $3 \text{ K cm s}^{-1}$  in October 2019, and reversals with negative values during January and February 2019. (Fig. 9f).

270 To further investigate the driving force behind the eddy temperature flux across the saddle in the weather-band, we analysed ensembles of events with high fluxes. In total 20 events with peaks  $(u_r', T') > 0$  and 24 events with peaks  $(u_r', T') < 0$  were detected, both resulting in positive eddy temperature fluxes. Most of these events occur during October, November, and December (red and blue triangles in Fig. 9e) when there is no sea ice in the area. The time series of 4-day duration centered at the selected time of each event are extracted. The ensemble-averaged records are denoted using angle brackets,  $\langle \cdot \rangle$  (Fig. 10).

275 The ensemble of events that satisfy the first condition is associated with southerly wind stress, resulting in an Ekman transport component that forces a positive current anomaly carrying positive temperature anomalies toward the east-southeast (Fig. 10a and 10c). The peak eddy temperature flux of  $(8.4 \pm 1.3) \text{ K cm s}^{-1}$  tends to occur one day after the maximum along-isobath

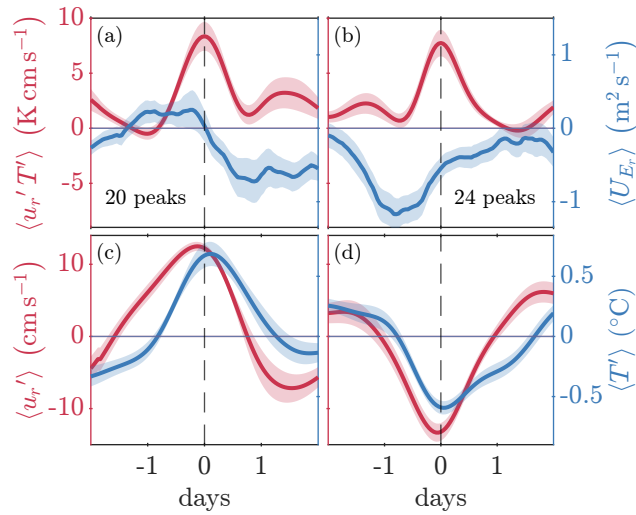


**Figure 10.** Ensemble-averaged time series for events with strong positive eddy temperature flux  $\langle u_r' T' \rangle$  (red) along the direction of highest variance ( $-28^\circ$ ) in the weather band (28 hours to 10 days) for the cases when  $(u_r', T') > 0$ , i.e., positive temperature anomalies are carried ESE by the current anomaly along isobath (a and c), and when  $(u_r', T') < 0$ , i.e., negative temperature anomalies are carried WNW by the current anomaly along isobath (b and d). The ensemble time series are (a–b)  $\langle u_r' T' \rangle$  (red), Ekman transport component along  $-28^\circ$ ,  $\langle U_{E_r} \rangle$  (blue), (c–d) current anomalies  $\langle u_r' \rangle$  (red) and temperature anomalies  $\langle T' \rangle$  (blue). The current anomalies are bin-averaged over the bottom half of the water column. The time axes (days) are centered at the peak of the eddy temperature flux. The standard error ( $SE = \text{std}(x)/\sqrt{n}$ , where  $n$  is the number of ensembles) is shown with shading.

Ekman transport. The temperature anomaly turns positive approximately half a day after the current anomaly, and their peaks are six hours apart.

280 The second case (Fig. 10b and 10d; events marked by blue triangles in Fig. 9e) corresponds to events when the wind from the north-northeast increases in strength, enhancing the Ekman transport opposing the current and resulting in a negative current anomaly carrying negative temperature anomalies toward west-northwest. The peak of eddy temperature flux reaches  $7.8(\pm 1.2) \text{ K cm s}^{-1}$ , approximately one day after the along-isobath Ekman transport component has reached its largest negative value. The temperature anomaly turns negative six hours after the current anomaly, and their peaks are two hours apart.

## 285 4 Discussion

### 4.1 Interannual versus seasonal variability – was 2018–2019 a typical year?

Several findings in the time series at the mooring position (Fig. 6) and the late-autumn hydrographic transects on the saddle (Fig. 5) warrant a discussion about the seasonal and interannual variability in the area and whether 2018–2019 was a typical year.



290 The autumns of 2018 and 2019 differed in hydrography and the onset of the sea ice period. During autumn 2018, the water  
column above the saddle remained warm and ice-free and was only partially covered with ice from December. In contrast,  
in autumn 2019, sea ice drifted to the saddle in late October, and the water cooled close to the freezing point in November.  
This suggests that the position of the ice cover in the Barents Sea during autumn affects the hydrographic conditions over the  
saddle at this time of the year. According to Kohlbach et al. (2023), the marginal ice zone had retreated beyond the shelf break  
295 and into the Nansen Basin in August 2018, while in August 2019, large parts of the northwestern Barents Sea shelf remained  
covered by sea ice, resulting in lower temperatures and a fresher surface layer. These differences in the large-scale conditions  
at the end of the melting seasons of 2018 and 2019 must also have affected the subsequent winter conditions at our mooring  
site. During the same autumns, observations in the Northern Barents Sea Opening showed a large difference in the upper ocean  
salinity accompanied by a similar difference in sea ice (Lundesgaard et al., 2022). Higher upper ocean freshening due to more  
300 sea ice melt can precondition the area for sea ice growth the following winter (Lind et al., 2018).

Superposed on the seasonal cycle, several episodes of warm water intrusions affected the sea ice cover at the saddle (Fig. 6b–  
c). The inflow of Atlantic-origin waters and heat transport onto the saddle are important for the onset and length of typical  
winter conditions. Strong current velocities directed across-saddle into the Barents Sea ( $u_R$ ) generally preceded the local  
temperature maxima associated with the warm water intrusions (Fig. 6c and 6d). Sea ice covered the mooring site starting  
305 from mid-January 2019, before the water column had completely cooled to the freezing point (Fig. 6b, c). Notwithstanding,  
favourable wind and ice conditions and geostrophic adjustment to the wind-driven Ekman transport from Edgeøya to Hopen  
resulted in depth-averaged currents reaching  $23 \text{ cm s}^{-1}$ , driving warmer waters from Storfjordrenna to the saddle. A similar  
response to wind forcing resulting in deep warm water overflow has also been observed on the sill in the inner part of Hornsund  
in Svalbard (Arntsen et al., 2019).

310 Not all warm inflow events are explained by the local wind effects, however. The event with the strong across-saddle current  
of  $30 \text{ cm s}^{-1}$  and the small increase in temperature, which occurred from mid-February to March, is likely caused by upstream  
conditions. Accelerating WSC and the branch going into Storfjordrenna can force the current to follow shallower isobaths to  
conserve potential vorticity (Nilsen et al., 2016). The small temperature increase during this period was most likely due to  
mixing of the warm water en route to the saddle. When the current subsided in early March, the temperature on the saddle  
315 returned to the freezing point, and the sea ice concentration increased to 90 %. Similarly, events during April with weaker  
current pulses transporting cooler waters can be attributed to forcing by the upstream conditions.

Northeasterly winds and relatively strong westward current reversals in the weeks before the November 2019 transect  
(Fig. 5a, Fig. 6a,d–e) likely imported sea ice and cooled the surface waters to the freezing point above the saddle. The large-  
scale sea ice cover was more extensive in November 2019 compared to November 2021. In 2019, the 15 % sea ice edge  
320 extended past Hopen, almost reaching the southern tip of Spitsbergen, while in 2021, it only extended south to Edgeøya and  
did not cover the Olga Basin (not shown). The higher temperature maximum and the alignment of the isohalines and isotherms  
in the transect from November 2021 (Fig. 5c) suggest an autumn inflow of Atlantic-origin water and an incomplete cooling  
of the water column. The SST in the region was substantially higher in 2021 compared to 2019, with the largest difference of

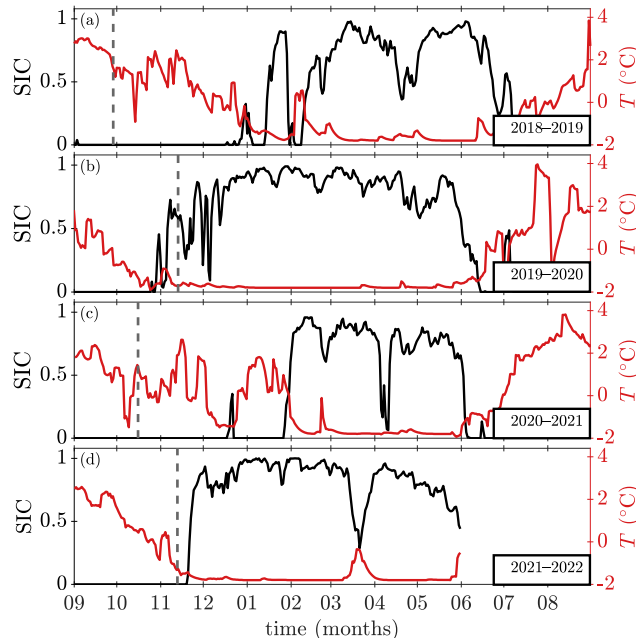


**Figure 11.** Sea ice concentration (black, left vertical axis) and sea surface temperature (red, right vertical axis) at the mooring location from September to September in a) 2018–2019, b) 2019–2020, c) 2020–2021, and d) 2021–2022. Dashed lines mark times of a) mooring deployment, b) mooring recovery and hydrographic transect in November 2019, c) hydrographic transect in October 2020, and d) hydrographic transect in November 2021. Sea ice concentration and sea surface temperature are taken from the OSTIA product (OSTIA, 2023; Good et al., 2020)).

325  $3^{\circ}\text{C}$  in Storfjordrenna (not shown), and  $1^{\circ}\text{C}$  to  $2^{\circ}\text{C}$  at the mooring position, so that the onset of freezing was delayed by one

The November transects (Fig. 5a,c) were both cooler and less saline than the October transect (Fig. 5b). This may be due to a regular seasonal shift from AW influence to Arctic Water influence at the site and/or interannual variability in this region. During autumn 2020, SST steadily decreased until rapidly increasing to  $1.4^{\circ}\text{C}$  during the week before the transect in mid-October (Fig. 11c). It then decreased to  $0^{\circ}\text{C}$  before increasing to  $2.6^{\circ}\text{C}$  in mid-November. Hence, autumn 2020 had warmer and longer-lasting overflows of water of Atlantic origin on the saddle and a later onset of sea ice than the other years. Atlantic inflow from the north of Svalbard has also been observed to affect the seasonal variability in local hydrography in the same way (Lundesgaard et al., 2022).

330 Autumn 2018 was comparable to autumn 2020 in terms of SST evolution at the mooring position (Fig. 11a and 11c). Inflow of warm water from Storfjordrenna maintained high SST above the saddle through November in both 2018 and 2020, and delayed the onset of sea ice in the subsequent winters.

In the context of the long-term changes in SST and SIC at the study site, the autumn 2018 to autumn 2019 (mooring year) was an average year in the recent two decades (not shown), and the difference between 2018 and 2019 was not remarkably

large. From 2005–06 and onwards, the interannual variability in SST and SIC at the mooring site was substantially higher than the previous 25 years, indicating that one might expect even larger year-to-year changes than what we observed between 2018 and 2019.

To summarise, strong interannual variability substantially impacts the seasonal cycle at the study site. Sea ice in the Barents Sea has a large interannual variability (e.g., Shi et al., 2024; Onarheim et al., 2024) driven by atmospheric temperature, sea surface temperature, and oceanic heat transport (Dörr et al., 2024). Locally, intrusions of warm water during autumn can delay the onset of winter conditions and inhibit local sea ice growth or melt imported sea ice, as observed in the autumns of 2018 and 2020 (Fig. 6b–c and 5b). These intrusions, whether driven by local winds or by upstream conditions, also frequently reduce the existing partial ice cover above the saddle during winter and spring (Fig. 11, earlier years not shown). This explains the differences in hydrographic conditions observed in November 2019 vs 2021 (Fig. 5a and 5c). The more persistent warm water overflow in 2020 likely delayed the seasonal watermass transformation and contributed to the October 2020 transect being substantially warmer than the November transects.

#### 4.2 Drivers of the mean exchange between Storfjordrenna and Barents Sea

The observed background current (10-day low-passed) tends to flow towards the southeast (Fig. 6c). This current direction is opposed by the geostrophic adjustment to the Ekman transport induced by the large-scale wind pattern from the northeast. The strength and direction of the current are affected by the wind stress, and in periods with strong winds, either reversed to northwestward flow or amplified in its normal southeastward direction (Fig. 8). Hence, the local wind is not the main driver of the background current on the saddle.

The forcing of the slowly varying current is more complex. We found a low and insignificant correlation between spatial differences in sea level and mooring current velocity, by analysing absolute dynamic topography and the associated geostrophic currents (not shown). This means either that the sea level slope locally is not the main driver of the current or that the data coverage and quality of the absolute dynamic topography measurements are not sufficiently good to show a clear relation. The quality of such measurements can be reduced due to seasonal ice coverage and the timing of the satellite passages, and the product quality north of the Arctic circle is not thoroughly tested (Oziel et al., 2020).

The current across the saddle may, on the other hand, be dependent on the strength of the current upstream in Storfjordrenna and on the slope west of Spitsbergenbanken (Sect. 4.1). Upstream, along the Norwegian coast, low-pressure systems accelerate the Norwegian Atlantic Current through onshore Ekman transport and set-up along the coast (Brown et al., 2023). However, it is unclear whether low-pressure systems would accelerate the WSC along the relatively shorter West-Spitsbergen coastline (Brown et al., 2023). Additionally, high variability in the tracks of low-pressure systems passing Svalbard (Wickström et al., 2020) makes the local wind influence west of Storfjordrenna and Svalbard highly variable. Current peaks at the mooring site are occasionally related to a strong WSC, quantified using the slope of absolute dynamic topography between Spitsbergenbanken and Storfjordrenna (not shown), generating a barotropic contribution to the current strength. Similar to the response of the WSC on the West Spitsbergen Shelf to anomalous wind stress curl (Nilsen et al., 2016), the branch of the WSC which flows

in Storfjordrenna can be displaced onto shallower isobaths. However, a more detailed analysis is needed to conclude on the effects of upstream forcing.

Another possible driver for the observed mean current is the tidal residual flow on Spitsbergenbanken. In shallow areas with strong tidal currents and non-linear bottom friction, residual currents may influence the circulation pattern (Harms, 1992).  
375 Tidally generated residual currents around Bjørnøya were reported from buoys (Vinje et al., 1989) and laboratory experiments and observations from drifters (McClimans and Nilsen, 1993). Several numerical model studies have shown that tidal rectification occurs in the region (Harms, 1992; Gjevik et al., 1994; Kowalik and Proshutinsky, 1995). Using higher-resolution models which better resolved nonlinear terms, strong anticyclonic tidal residual current was reported around Bjørnøya and on Spitsbergenbanken (reaching  $15 \text{ cm s}^{-1}$ ) and around Hopen (Kowalik and Marchenko, 2023). Simulations have reproduced the  
380 anticyclonic drift of buoys around Hopen, which is driven by strong tidal currents caused by interaction between the semidiurnal tide and the island of Hopen (Marchenko and Kowalik, 2023).

### 4.3 Tidal-, weather- and low-frequency band variability and their impact on the eastward heat transport into the Olga Basin

Both semidiurnal and diurnal tidal currents contribute to the transport of heat across the saddle on Hopenbanken, with the  
385 semidiurnal contribution being significantly larger. The semi-major axis of the semidiurnal currents is oriented along  $20^\circ$ , i.e. roughly east-northeast, which is roughly perpendicular to the eddy temperature flux in the semidiurnal band (Fig. 9). The direction of the eddy temperature flux is mainly in the southeast sector for all the frequency bands. This is likely due to the position of the temperature gradient on the saddle and the guiding of the current anomalies by topography.

The oscillations on timescales between one and six weeks result in sporadic moderate eddy temperature fluxes in the south-  
390 east sector, comparable to the semidiurnal band in magnitude, but more variable in direction. The largest contribution towards east-southeast was during autumn 2019 (Fig. 9f), when the wavelet transform of  $u_r$  (Fig. 7b), and especially of  $T_b$  (Fig. 7e), had power in the low-frequency area, implying that the varying current brought even larger temperature variations. These concurrent fluctuations added up to a considerable eddy temperature flux in this period. We hypothesise that the high eddy temperature flux this autumn may be caused by AW upstream of the saddle being lifted onto shallower isobaths due to either regional Ek-  
395 man pumping or an acceleration of the upstream current system, resulting in higher temperatures on one side of the front on the saddle. Locally at the mooring site, this was observed as low-frequency oscillations with particularly high-temperature variations causing a large eddy temperature flux into the Barents Sea.

Integrated over the measurement period, the weather band eddy temperature flux was approximately twice that of the low-frequency and the semidiurnal bands, both of which had comparable magnitudes. During the period with a relatively high sea  
400 ice coverage, from February through July, the semidiurnal tide leads twice as much heat across the saddle as the weather band and 1.5 times as much as the band associated with mesoscale activity.

Eddy temperature fluxes calculated in Section 3.6 contain both their divergent and rotational components. Only the divergent part plays a part in the actual transport of heat across the saddle (Marshall and Shutts, 1981; Guo et al., 2014). Using our data

set we cannot separate the contribution of the divergent or rotational eddy temperature fluxes, hence, the values must be taken  
405 as an upper bound.

#### **4.4 Consequences of the long-term changes in the hydrographic environment in Storfjordrenna for the heat transport into the Barents Sea**

In recent years, the AW presence in Storfjordrenna upstream of the study site has increased. Storfjordrenna is among the locations in the Barents Sea that have experienced the highest increase in sea surface temperature over the last two decades  
410 (Barton et al., 2018; Bayoumy et al., 2022b). The climatology in Storfjordrenna (Section 3.1) also shows that the water column has become warmer since 2000 compared to previous years (Fig. 3), and that Atlantic-origin water has shoaled and now reaches further east towards the saddle during summer (Fig. 4). The shoaling of AW has also been observed in the Eurasian Arctic (Polyakov et al., 2017), along the coast and in the fjords of West-Spitsbergen (Tverberg et al., 2019; Skogseth et al., 2020; Strzelewicz et al., 2022). Additionally, AW advected into the fjords in West-Spitsbergen has warmed in the recent two  
415 decades (Bloskhina et al., 2021; Pavlov et al., 2013; Tverberg et al., 2019; Skogseth et al., 2020). At the mooring site, the years after 2005–06 had on average higher mean annual SST and fewer days of sea ice coverage compared to the years between 1981–82 and 2004–05 (not shown), which may be due to increased AW inflows in the Barents Sea compared to Fram Strait after 2006 (Polyakov et al., 2023). The warmest year was 2015–16, with abnormally high mean SST above the saddle and only 106 days of any sea ice and no SIC above 0.8. This was the same year when Storfjordrenna, along with the Barents Sea in  
420 general (Bayoumy et al., 2022b), experienced a record-low sea ice cover and a warm, saline surface layer (Vivier et al., 2023), and a record-warm and long-lasting marine heatwave (Bayoumy et al., 2022a).

As the AW circulates over shallower isobaths, the physical processes in the channel between Storfjordrenna and the Olga Basin may more easily transport heat eastward in the future. Anomalous wind stress curl can affect the circulation depth of AW in Storfjordrenna and therefore lead AW or Atlantic-origin waters closer to the saddle between Storfjordrenna and the Olga  
425 Basin (Sect. 4.2).

Several factors determine the fate of warm waters crossing the saddle. The circulation pattern in the channel and downstream affects whether Atlantic-origin water is transported to the Arctic or the Atlantic side of the Polar Front, which follows the 200 m isobath separating the Olga Basin from Hopen djupet (Fig. 2). While the time-averaged flow observed by the mooring was directed towards the southeast, with most non-tidal variability contributing to heat exchange occurring along the west-northwest  
430 to east-southeast axis (Sections 3.4, 3.5, 3.6), the complex bathymetry in the region and limitations in our observations prevent a definitive conclusion regarding the specific path of the AW or the fraction of heat that could contribute to the heat budget on the northern side of the Polar Front. Nonetheless, the AW transport through the channel between Storfjordrenna and the Olga Basin has the potential to impact the Olga Basin, which still has a seasonal ice cover and a cold, thick layer of Arctic Water (e.g., Lind and Ingvaldsen, 2012).

435 Given the possibility that Atlantic-origin waters from Storfjordrenna may be transported into the Arctic side of the Polar Front east of Hopenbanken, the density stratification within the Olga Basin becomes an important factor in determining the consequences of this transport for the local conditions. Denser waters on the eastern side would cause Atlantic-origin waters

to penetrate at shallower depths, impacting the winter and spring sea ice cover and generally depositing more heat into the upper water column, with implications for the sea ice growth in the subsequent season. Conversely, less dense waters on the eastern side could cause subduction of the overflow waters. If pure AW, or water with properties closer to AW than what was observed in this study, flows over the saddle, its density can exceed that of the local water in the Olga Basin (Arctic Water, East Spitsbergen Water) and thereby contribute to the deeper stratification. We noted the deepening of the  $34.4 \text{ g kg}^{-1}$  isobath and a small decrease in temperature in parts of the Olga Basin (Fig. 4b–c) in the recent two decades. However, due to the particularly sparse data coverage in the Olga Basin, we are cautious about interpreting these changes.

Atlantic-origin waters reaching the saddle between Storfjordrenna and the Barents Sea will influence the properties of the East Spitsbergen Current flowing into Storfjorden. More AW mixed into the East Spitsbergen Current on the saddle will have consequences for the Coastal Current in Storfjorden and along the west coast of Spitsbergen, as well as the exchange between the shelf and the fjords. It will also affect the dense water production in Storfjorden and subsequent deep water export to Fram Strait, as the initial salinity of the source water preconditions the density of the overflow (Schauer, 1995; Skogseth et al., 2004; Vivier et al., 2023).

## 5 Conclusions

We have used available historical hydrographic profiles to study changes in the hydrographic environment in Storfjordrenna, the shallow banks around, and in the Olga Basin north of the Polar Front in the recent two decades compared to 1930–2000. In addition, we analysed recent late-autumn hydrographic transects and a year-long time series of near-bottom hydrography and water column current velocity on the saddle separating Storfjordrenna from the Olga Basin between Edgeøya and Hopen islands.

The mooring observations show that AW and Atlantic-origin waters in Storfjordrenna can cross the saddle and enter the Arctic domain of the northwestern Barents Sea. The across-saddle current is mediated by wind forcing. Southerly winds over the saddle cause stronger currents into the Barents Sea and are associated with events of strong eddy temperature flux. The pronounced semidiurnal tidal currents over the saddle also contribute to heat transport into the Barents Sea, about half of the wind-driven flux. The area is characterised by large seasonal and interannual variability in hydrography and sea ice cover and frequent intrusions of warm water from Storfjordrenna. Both local wind stress and upstream conditions can force these intrusions, and they are important for the onset and length of typical winter conditions in the area.

The two recent decades were warmer and more influenced by AW in the Atlantic sector of the northwestern Barents Sea. This increase in heat in the Atlantic sector, potential shoaling of AW, and the ongoing changes in large-scale wind patterns would indicate that the channel separating Storfjordrenna from the Barents Sea may emerge as an important pathway of AW and heat into the Arctic sector of the Barents Sea in the future. The complex interplay of local and non-local processes governing the large variability of AW inflow on seasonal to interannual timescales warrants more comprehensive data collection and analysis in this area.

470 *Data availability.* The mooring data can temporarily be retrieved from <https://figshare.com/s/e4f2c67e8df9f68d306b>. This data set will be published in the Norwegian Marine Data Centre. Hydrographic data (Skogseth et al., 2019) used for the climatological sections can be retrieved from <https://data.npolar.no/dataset/39d9f0f9-af12-420c-a879-10990df2e22d>. Hydrographic data from the cruise in 2019 (Sundfjord, 2022) are available through <https://metadata.nmdc.no/metadata-api/landingpage/b62edd66b56570a4374fd790bc8be3b9>, the cruise in 2020 (Fer, 2020) through <https://metadata.nmdc.no/metadata-api/landingpage/269c4764094da6b5a4434fd27d983620>, and the cruise in 475 2021 (Sundfjord, 2023) from <https://metadata.nmdc.no/metadata-api/landingpage/2609bab822f8921a173287a6a3c92b65>. ERA5 reanalyses (Hersbach et al., 2020) are available from <https://cds.climate.copernicus.eu/cdsapp#!/dataset/reanalysis-era5-single-levels>. The Global Ocean OSTIA Sea Surface Temperature and Sea Ice Reprocessed product (OSTIA, 2023; Good et al., 2020) is available from [https://data.marine.copernicus.eu/product/SST\\_GLO\\_SST\\_L4\\_REP\\_OBSERVATIONS\\_010\\_011/description](https://data.marine.copernicus.eu/product/SST_GLO_SST_L4_REP_OBSERVATIONS_010_011/description).

## Appendix A: Methodology for the climatological hydrography maps and sections

480 The historical hydrographic data have been optimally interpolated onto horizontal and vertical climatological sections to compare the two recent decades to earlier decades. The interpolation was done using the kriging algorithm in Golden Software Surfer 12 through the MATLAB function `surfergriddata.m` (point kriging with no drift, linear variogram model with unit slope and anisotropy). The spatial resolution of bin averages before kriging is described in section 4.2–4.3 of Skogseth et al. (2020). Due to temporally and spatially sparse data coverage, only summer (July–October mean) sections were possible to create. For 485 the period 1930–2000, if a bin had data from fewer than three years, that bin was retained without data to ensure an unbiased representation. For the period 2000–2019, this minimum threshold was lowered to one year to ensure enough data to produce the kriging-interpolated sections. Data coverage and standard deviations for the horizontal climatological sections are shown in Fig. A2 and Fig. A1 and for the vertical climatological sections in Fig. A4 and Fig. A3.

Vertical climatological sections of summertime (July–October) temperature and salinity over the periods 1930–2000 and 490 2000–2019 were made from hydrographic profiles within  $\pm 0.15^\circ$  perpendicular distance from an along-section from Storfjordrenna across the saddle and into the Olga Basin, comprised by the bin centres shown in Fig. 3a to where the profiles were first bin-averaged. The bin sizes in the along-section direction were the half between two neighboring bin centres. At the end points of the sections, profiles within  $0.3^\circ$  west (east) of the western (eastern) bin centre were included in the bin average. Each profile was weighted with its distance to the bin centre to produce weighted bin-averaged sections with 5 m vertical resolution. 495 The weighted bin-averaged sections were then interpolated onto a 500 m horizontal times 5 m vertical grid resolution using kriging interpolation.

Similarly, weighted bin-averaged horizontal distributions of depth-averaged temperature and salinity over the whole water column were estimated on a  $0.5^\circ$  longitude times  $0.2^\circ$  latitude grid resolution for the area  $20^\circ$  E– $28^\circ$  E;  $76^\circ$  N– $78^\circ$  N, where each profile was weighted with its distance from the bin centre it belonged to. The weighted bin-averaged depth-averaged 500 temperature and salinity horizontal sections were then interpolated onto a 2 times finer grid using the kriging interpolation method described above. In both grids the land points were excluded.

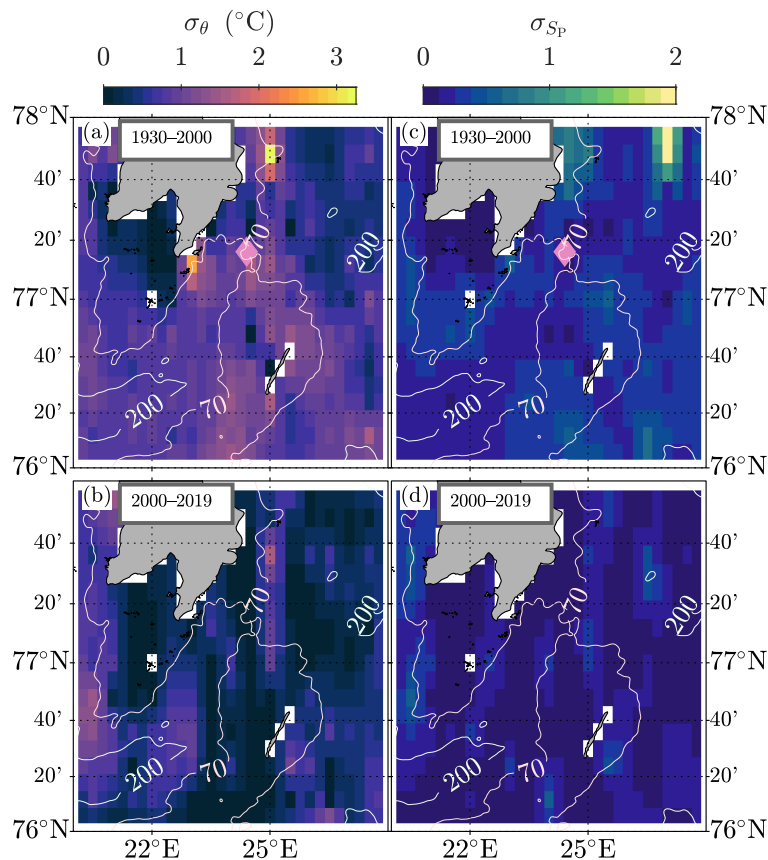


**Figure A1.** Standard deviations of the climatological horizontal hydrographic depth-averaged maps (Fig. 3). a–b) Standard deviation of potential temperature  $\sigma_{\theta}$  ( $^{\circ}\text{C}$ ), c–d) standard deviation of practical salinity  $\sigma_{S_p}$ . a, c) 1930–2000, b, d) 2000–2019. The 70 m and 200 m isobaths are shown in white contours. The mooring location is indicated with a pink diamond.

*Author contributions.* RS designed the study. KK and IF processed the mooring current velocity data. KK processed the mooring hydrographic data and the recent autumn and winter hydrographic data. RS compiled historical hydrographic data and made the climatological sections. KK analysed the data, prepared the figures and drafted the manuscript. RS wrote the text in the appendix. All authors have contributed to discussing the material and giving input and feedback on the analysis and the manuscript in several stages.

*Competing interests.* At least one of the (co-)authors is a member of the editorial board of Ocean Science.

*Acknowledgements.* This work was funded by the Research Council of Norway through the project The Nansen Legacy (RCN # 276730). The authors are grateful for the cooperation with the crew and the scientific/technical colleagues onboard the research vessels *Kronprins*



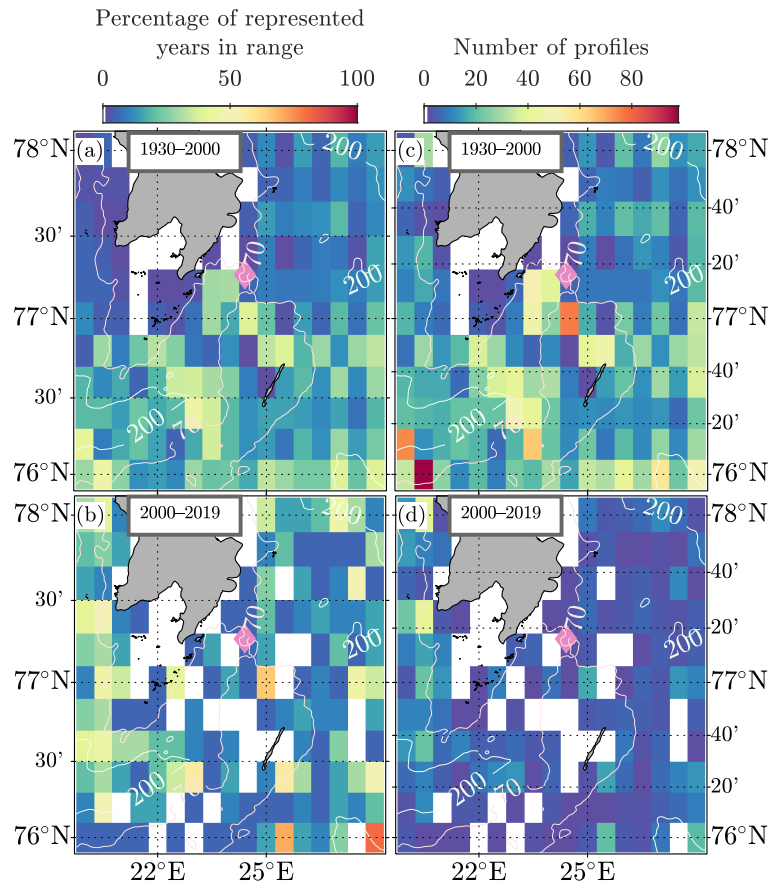


**Figure A2.** Data coverage of the climatological horizontal hydrographic depth-averaged maps (Fig. 3). Percentage of years with at least one profile in a) 1930–2000, b) 2000–2019, and number of profiles in c) 1930–2000, d) 2000–2019. The 70 m and 200 m isobaths are shown in white contours. The mooring location is indicated with a pink diamond.

510 *Haakon and G. O. Sars.* We thank colleagues who have read the manuscript, discussed the material, and provided feedback on the study. We thank the two anonymous referees whose constructive feedback improved the manuscript.

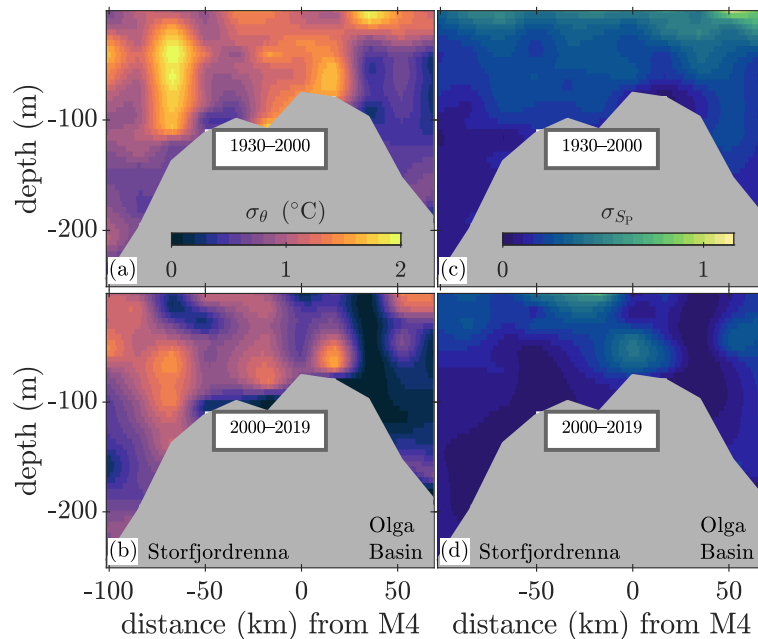


**Figure A3.** Standard deviations of the climatological vertical hydrographic transects (Fig. 4). a–b) Standard deviation of potential temperature  $\sigma_{\theta}$  ( $^{\circ}\text{C}$ ), c–d) standard deviation of practical salinity  $\sigma_{S_p}$ . a, c) 1930–2000, b, d) 2000–2019. Horizontal axis shows distance to the mooring position, with positive values towards the Olga Basin. The location of the section is indicated with green dots in Fig. 3a.

## References

- Arntsen, M., Sundfjord, A., Skogseth, R., Błaszczuk, M., and Promińska, A.: Inflow of Warm Water to the Inner Hornsund Fjord, Svalbard: Exchange Mechanisms and Influence on Local Sea Ice Cover and Glacier Front Melting, *Journal of Geophysical Research: Oceans*, 124, 1915–1931, <https://doi.org/10.1029/2018JC014315>, 2019.
- 515 Årthun, M. and Schrum, C.: Ocean Surface Heat Flux Variability in the Barents Sea, *Journal of Marine Systems*, 83, 88–98, <https://doi.org/10.1016/j.jmarsys.2010.07.003>, 2010.
- Årthun, M., Ingvaldsen, R. B., Smedsrud, L. H., and Schrum, C.: Dense Water Formation and Circulation in the Barents Sea, *Deep-Sea Research Part I: Oceanographic Research Papers*, 58, 801–817, <https://doi.org/10.1016/j.dsr.2011.06.001>, 2011.
- Årthun, M., Eldevik, T., Smedsrud, L. H., Skagseth, Ø., and Ingvaldsen, R. B.: Quantifying the Influence of Atlantic Heat on Barents Sea Ice Variability and Retreat\*, *Journal of Climate*, 25, 4736–4743, <https://doi.org/10.1175/JCLI-D-11-00466.1>, 2012.
- 520 Årthun, M., Onarheim, I. H., Dörr, J., and Eldevik, T.: The Seasonal and Regional Transition to an Ice-Free Arctic, *Geophysical Research Letters*, 48, e2020GL090825, <https://doi.org/10.1029/2020GL090825>, 2021.
- Asbjørnsen, H., Årthun, M., Skagseth, Ø., and Eldevik, T.: Mechanisms Underlying Recent Arctic Atlantification, *Geophysical Research Letters*, 47, e2020GL088036, <https://doi.org/10.1029/2020GL088036>, 2020.
- 525 Barton, B. I., Lenn, Y.-D., and Lique, C.: Observed Atlantification of the Barents Sea Causes the Polar Front to Limit the Expansion of Winter Sea Ice, *Journal of Physical Oceanography*, 48, 1849–1866, <https://doi.org/10.1175/jpo-d-18-0003.1>, 2018.

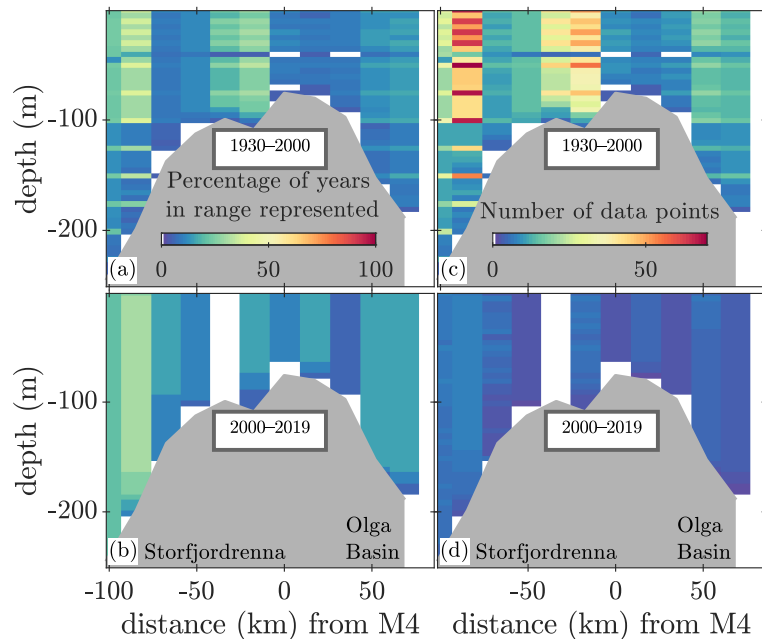


**Figure A4.** Data coverage of the climatological vertical hydrographic transects (Fig. 4). a–b) Percentage of years represented in a) 1930–2000, b) 2000–2019, and number of data points in c) 1930–2000, d) 2000–2019. Horizontal axis shows distance to the mooring position, with positive values towards the Olga Basin. The location of the section is indicated with green dots in Fig. 3a.

Bayoumy, M., Nilsen, F., and Skogseth, R.: Marine Heatwaves Characteristics in the Barents Sea Based on High Resolution Satellite Data (1982–2020), *Frontiers in Marine Science*, 9, 2022a.

530 Bayoumy, M., Nilsen, F., and Skogseth, R.: Interannual and Decadal Variability of Sea Surface Temperature and Sea Ice Concentration in the Barents Sea, *Remote Sensing*, 14, 4413, <https://doi.org/10.3390/rs14174413>, 2022b.

Bloshkina, E. V., Pavlov, A. K., and Filchuk, K.: Warming of Atlantic Water in Three West Spitsbergen Fjords: Recent Patterns and Century-Long Trends, *Polar Research*, 40, <https://doi.org/10.33265/polar.v40.5392>, 2021.

Brown, N. J., Mauritzen, C., Li, C., Madonna, E., Isachsen, P. E., and LaCasce, J. H.: Rapid Response of the Norwegian Atlantic Slope Current to Wind Forcing, *Journal of Physical Oceanography*, 53, 389–408, <https://doi.org/10.1175/JPO-D-22-0014.1>, 2023.

535 Dalpadado, P., Arrigo, K. R., van Dijken, G. L., Skjoldal, H. R., Bagøien, E., Dolgov, A. V., Prokopchuk, I. P., and Sperfeld, E.: Climate Effects on Temporal and Spatial Dynamics of Phytoplankton and Zooplankton in the Barents Sea, *Progress in Oceanography*, 185, 102 320, <https://doi.org/10.1016/j.pocean.2020.102320>, 2020.

Dickson, RR., Midttun, L., and Mukhin, AI.: The Hydrographic Conditions in the Barents Sea in August–September 1965–1968, *International 0-group fish surveys in the Barents Sea*, 18, 3–24, <https://doi.org/10.17895/ices.pub.8051>, 1970.

540 Dörr, J., Årthun, M., Docquier, D., Li, C., and Eldevik, T.: Causal Links Between Sea-Ice Variability in the Barents-Kara Seas and Oceanic and Atmospheric Drivers, *Geophysical Research Letters*, 51, e2024GL108 195, <https://doi.org/10.1029/2024GL108195>, 2024.

Eriksen, E., Skjoldal, H. R., Gjørseter, H., and Primicerio, R.: Spatial and Temporal Changes in the Barents Sea Pelagic Compartment during the Recent Warming, *Progress in Oceanography*, 151, 206–226, <https://doi.org/10.1016/j.pocean.2016.12.009>, 2017.

- Eriksen, E., Gjørseter, H., Prozorkevich, D., Shamray, E., Dolgov, A., Skern-Mauritzen, M., Stiansen, J. E., Kovalev, Y., and Sunnanå, K.: From Single Species Surveys towards Monitoring of the Barents Sea Ecosystem, *Progress in Oceanography*, 166, 4–14, <https://doi.org/10.1016/j.pocean.2017.09.007>, 2018.
- Erofeeva, S. and Egbert, G.: Arc5km2018: Arctic Ocean Inverse Tide Model on a 5 Kilometer Grid, 2018, <https://doi.org/10.18739/A21R6N14K>, 2020.
- Fer, I.: Physical Oceanography Data from the Cruise KB 2018616 with R.V. Kristine Bonnevie., <https://doi.org/10.21335/NMDC-2047975397>, 2020.
- Fer, I., Skogseth, R., Astad, S. S., Baumann, T., Elliott, F., Falck, E., Gawinski, C., and Kolås, E. H.: SS-MS2 Process Cruise/Mooring Service 2020: Cruise Report, The Nansen Legacy Report Series, <https://doi.org/10.7557/nlrs.5798>, 2021.
- Geoffroy, M., Berge, J., Majaneva, S., Johnsen, G., Langbehn, T. J., Cottier, F., Mogstad, A. A., Zolich, A., and Last, K.: Increased Occurrence of the Jellyfish *Periphylla periphylla* in the European High Arctic, *Polar Biology*, 41, 2615–2619, <https://doi.org/10.1007/s00300-018-2368-4>, 2018.
- Gerland, S., Ingvaldsen, R. B., Reigstad, M., Sundfjord, A., Bogstad, B., Chierici, M., Hop, H., Renaud, P. E., Smedsrud, L. H., Stige, L. C., Årthun, M., Berge, J., Bluhm, B. A., Borgå, K., Bratbak, G., Divine, D. V., Eldevik, T., Eriksen, E., Fer, I., Fransson, A., Gradinger, R., Granskog, M. A., Haug, T., Husum, K., Johnsen, G., Jonassen, M. O., Jørgensen, L. L., Kristiansen, S., Larsen, A., Lien, V. S., Lind, S., Lindstrøm, U., Mauritzen, C., Melsom, A., Mernild, S. H., Müller, M., Nilsen, F., Primicerio, R., Søreide, J. E., van der Meeren, G. I., and Wassmann, P.: Still Arctic?—The Changing Barents Sea, *Elementa: Science of the Anthropocene*, 11, 00088, <https://doi.org/10.1525/elementa.2022.00088>, 2023.
- Gjevik, B., Nøst, E., and Straume, T.: Model Simulations of the Tides in the Barents Sea, *Journal of Geophysical Research*, 99, 3337, <https://doi.org/10.1029/93JC02743>, 1994.
- Good, S., Fiedler, E., Mao, C., Martin, M. J., Maycock, A., Reid, R., Roberts-Jones, J., Searle, T., Waters, J., While, J., and Worsfold, M.: The Current Configuration of the OSTIA System for Operational Production of Foundation Sea Surface Temperature and Ice Concentration Analyses, *Remote Sensing*, 12, 720, <https://doi.org/10.3390/rs12040720>, 2020.
- Guo, C., Ilicak, M., Fer, I., Darelus, E., and Bentsen, M.: Baroclinic Instability of the Faroe Bank Channel Overflow, *Journal of Physical Oceanography*, 44, 2698–2717, <https://doi.org/10.1175/JPO-D-14-0080.1>, 2014.
- Häkkinen, S. and Cavalieri, D. J.: A Study of Oceanic Surface Heat Fluxes in the Greenland, Norwegian, and Barents Seas, *Journal of Geophysical Research: Oceans*, 94, 6145–6157, <https://doi.org/10.1029/JC094iC05p06145>, 1989.
- Harms, I. H.: A Numerical Study of the Barotropic Circulation in the Barents and Kara Seas, *Continental Shelf Research*, 12, 1043–1058, [https://doi.org/10.1016/0278-4343\(92\)90015-C](https://doi.org/10.1016/0278-4343(92)90015-C), 1992.
- Hersbach, H., Bell, B., Berrisford, P., Hirahara, S., Horányi, A., Muñoz-Sabater, J., Nicolas, J., Peubey, C., Radu, R., Schepers, D., Simmons, A., Soci, C., Abdalla, S., Abellan, X., Balsamo, G., Bechtold, P., Biavati, G., Bidlot, J., Bonavita, M., De Chiara, G., Dahlgren, P., Dee, D., Diamantakis, M., Dragani, R., Flemming, J., Forbes, R., Fuentes, M., Geer, A., Haimberger, L., Healy, S., Hogan, R. J., Hólm, E., Janisková, M., Keeley, S., Laloyaux, P., Lopez, P., Lupu, C., Radnoti, G., de Rosnay, P., Rozum, I., Vamborg, F., Villaume, S., and Thépaut, J.-N.: The ERA5 Global Reanalysis, *Quarterly Journal of the Royal Meteorological Society*, 146, 1999–2049, <https://doi.org/10.1002/qj.3803>, 2020.
- Ingvaldsen, R. B., Assmann, K. M., Primicerio, R., Fossheim, M., Polyakov, I. V., and Dolgov, A. V.: Physical Manifestations and Ecological Implications of Arctic Atlantification, *Nature Reviews Earth & Environment*, 2, 874–889, <https://doi.org/10.1038/s43017-021-00228-x>, 2021.

- Isaksen, K., Nordli, Ø., Ivanov, B., Køltzow, M. A. Ø., Aaboe, S., Gjeltten, H. M., Mezghani, A., Eastwood, S., Førland, E., Benestad, R. E., Hanssen-Bauer, I., Brækkan, R., Sviashchennikov, P., Demin, V., Revina, A., and Karandasheva, T.: Exceptional Warming over the Barents Area, *Scientific Reports*, 12, 9371, <https://doi.org/10.1038/s41598-022-13568-5>, 2022.
- 585 Ivanov, V. V., Frolov, I. E., and Filchuk, K. V.: Transformation of Atlantic Water in the North-Eastern Barents Sea in Winter, *Arctic and Antarctic Research*, 66, 246–266, <https://doi.org/10.30758/0555-2648-2020-66-3-246-266>, 2020.
- Jakobsson, M., Mayer, L., Coakley, B., Dowdeswell, J. A., Forbes, S., Fridman, B., Hodnesdal, H., Noormets, R., Pedersen, R., Rebesco, M., Schenke, H. W., Zarayskaya, Y., Accettella, D., Armstrong, A., Anderson, R. M., Bienhoff, P., Camerlenghi, A., Church, I., Edwards, M., Gardner, J. V., Hall, J. K., Hell, B., Hestvik, O., Kristoffersen, Y., Marcussen, C., Mohammad, R., Mosher, D., Nghiem, S. V., Pedrosa, 590 M. T., Travaglini, P. G., and Weatherall, P.: The International Bathymetric Chart of the Arctic Ocean (IBCAO) Version 3.0, *Geophysical Research Letters*, 39, n/a–n/a, <https://doi.org/10.1029/2012GL052219>, 2012.
- Jakobsson, M., Mayer, L. A., Bringensparr, C., Castro, C. F., Mohammad, R., Johnson, P., Ketter, T., Accettella, D., Amblas, D., An, L., Arndt, J. E., Canals, M., Casamor, J. L., Chauché, N., Coakley, B., Danielson, S., Demarte, M., Dickson, M. L., Dorschel, B., Dowdeswell, J. A., Dreutter, S., Fremand, A. C., Gallant, D., Hall, J. K., Hehemann, L., Hodnesdal, H., Hong, J., Ivaldi, R., Kane, E., Klauke, I., Krawczyk, 595 D. W., Kristoffersen, Y., Kuipers, B. R., Millan, R., Masetti, G., Morlighem, M., Noormets, R., Prescott, M. M., Rebesco, M., Rignot, E., Semiletov, I., Tate, A. J., Travaglini, P., Velicogna, I., Weatherall, P., Weinrebe, W., Willis, J. K., Wood, M., Zarayskaya, Y., Zhang, T., Zimmermann, M., and Zinglensen, K. B.: The International Bathymetric Chart of the Arctic Ocean Version 4.0, *Scientific Data*, 7, 1–14, <https://doi.org/10.1038/s41597-020-0520-9>, 2020.
- Knipowitsch, N.: Hydrologische Untersuchungen Im Europäischen Eismeer, *Annalen der Hydrographie und Maritimen Meteorologie*, 33, 600 241–260, 1905.
- Kohlbach, D., Goragner, L., Bodur, Y., Müller, O., Amargant Arumí, M., Blix, K., Bratbak, G., Chierici, M., Dąbrowska, A., Dietrich, U., Edvardsen, B., García, L., Gradinger, R., Hop, H., Jones, E., Lundesgaard, Ø., Olsen, L., Reigstad, M., Saubrekka, K., and Assmy, P.: Earlier Sea-Ice Melt Extends the Oligotrophic Summer Period in the Barents Sea with Low Algal Biomass and Associated Low Vertical Flux, *Progress in Oceanography*, p. 103018, <https://doi.org/10.1016/j.pocean.2023.103018>, 2023.
- 605 Kolås, E. H., Baumann, T. M., Skogseth, R., Koenig, Z., and Fer, I.: Western Barents Sea Circulation and Hydrography, Past and Present, <https://doi.org/10.22541/essoar.169203078.81082540/v1>, 2023.
- Kowalik, Z. and Marchenko, A.: Tidal Motion Enhancement on Spitsbergen Bank, Barents Sea, *Journal of Geophysical Research: Oceans*, 128, e2022JC018 539, <https://doi.org/10.1029/2022JC018539>, 2023.
- Kowalik, Z. and Proshutinsky, A. Yu.: Topographic Enhancement of Tidal Motion in the Western Barents Sea, *Journal of Geophysical 610 Research: Oceans*, 100, 2613–2637, <https://doi.org/10.1029/94JC02838>, 1995.
- Lewis, K. M., van Dijken, G. L., and Arrigo, K. R.: Changes in Phytoplankton Concentration Now Drive Increased Arctic Ocean Primary Production, *Science*, 369, 198–202, <https://doi.org/10.1126/science.aay8380>, 2020.
- Lilly, J. M. and Olhede, S. C.: Wavelet Ridge Estimation of Jointly Modulated Multivariate Oscillations, in: 2009 Conference Record of the Forty-Third Asilomar Conference on Signals, Systems and Computers, pp. 452–456, IEEE, Pacific Grove, CA, USA, ISBN 978-1-4244- 615 5825-7, <https://doi.org/10.1109/ACSSC.2009.5469858>, 2009.
- Lind, S. and Ingvaldsen, R. B.: Variability and Impacts of Atlantic Water Entering the Barents Sea from the North, *Deep Sea Research Part I: Oceanographic Research Papers*, 62, 70–88, <https://doi.org/10.1016/j.dsr.2011.12.007>, 2012.
- Lind, S., Ingvaldsen, R. B., and Furevik, T.: Arctic Warming Hotspot in the Northern Barents Sea Linked to Declining Sea-Ice Import, *Nature Climate Change*, 8, 634–639, <https://doi.org/10.1038/s41558-018-0205-y>, 2018.

- 620 Loeng, H.: Features of the Physical Oceanographic Conditions of the Barents Sea, *Polar Research*, 10, 5–18, <https://doi.org/10.1111/j.1751-8369.1991.tb00630.x>, 1991.
- Lundesgaard, Ø., Sundfjord, A., Lind, S., Nilsen, F., and Renner, A. H. H.: Import of Atlantic Water and Sea Ice Controls the Ocean Environment in the Northern Barents Sea, *Ocean Science*, 18, 1389–1418, <https://doi.org/10.5194/os-18-1389-2022>, 2022.
- Lüpkes, C. and Birnbaum, G.: ‘Surface Drag in the Arctic Marginal Sea-ice Zone: A Comparison of Different Parameterisation Concepts’, *Boundary-Layer Meteorology*, 117, 179–211, <https://doi.org/10.1007/s10546-005-1445-8>, 2005.
- 625 Marchenko, A. and Kowalik, Z.: Tidal Wave–Elliptic Island Interaction above the Critical Latitude, *Journal of Physical Oceanography*, 53, 683–698, <https://doi.org/10.1175/JPO-D-22-0018.1>, 2023.
- Marshall, J. and Shutts, G.: A Note on Rotational and Divergent Eddy Fluxes, *Journal of Physical Oceanography*, 11, 1677–1680, [https://doi.org/10.1175/1520-0485\(1981\)011<1677:ANORAD>2.0.CO;2](https://doi.org/10.1175/1520-0485(1981)011<1677:ANORAD>2.0.CO;2), 1981.
- 630 McClimans, T. A. and Nilsen, J. H.: Laboratory Simulation of the Ocean Currents in the Barents Sea, *Dynamics of Atmospheres and Oceans*, 19, 3–25, [https://doi.org/10.1016/0377-0265\(93\)90030-B](https://doi.org/10.1016/0377-0265(93)90030-B), 1993.
- Mcdougall, T. J. and Krzysik, O. A.: Spiciness, *Journal of Marine Research*, 73, 141–152, 2015.
- Midttun, L.: Formation of Dense Bottom Water in the Barents Sea, *Deep Sea Research Part A. Oceanographic Research Papers*, 32, 1233–1241, [https://doi.org/10.1016/0198-0149\(85\)90006-8](https://doi.org/10.1016/0198-0149(85)90006-8), 1985.
- 635 Nilsen, F., Skogseth, R., Vaardal-Lunde, J., and Inall, M.: A Simple Shelf Circulation Model: Intrusion of Atlantic Water on the West Spitsbergen Shelf, *Journal of Physical Oceanography*, 46, 1209–1230, <https://doi.org/10.1175/JPO-D-15-0058.1>, 2016.
- Olhede, S. and Walden, A.: Generalized Morse Wavelets, *IEEE Transactions on Signal Processing*, 50, 2661–2670, <https://doi.org/10.1109/TSP.2002.804066>, 2002.
- Onarheim, I. H. and Årthun, M.: Toward an Ice-Free Barents Sea, *Geophysical Research Letters*, 44, 8387–8395, <https://doi.org/10.1002/2017GL074304>, 2017.
- 640 Onarheim, I. H., Årthun, M., Teigen, S. H., Eik, K. J., and Steele, M.: Recent Thickening of the Barents Sea Ice Cover, *Geophysical Research Letters*, 51, e2024GL108225, <https://doi.org/10.1029/2024GL108225>, 2024.
- OSTIA: Global Ocean OSTIA Sea Surface Temperature and Sea Ice Reprocessed, <https://doi.org/10.48670/moi-00168>, 2023.
- Oziel, L., Sirven, J., and Gascard, J.-C.: The Barents Sea Frontal Zones and Water Masses Variability (1980–2011), *Ocean Science*, 12, 169–184, <https://doi.org/10.5194/os-12-169-2016>, 2016.
- 645 Oziel, L., Baudena, A., Ardyna, M., Massicotte, P., Randelhoff, A., Sallée, J.-B., Ingvaldsen, R. B., Devred, E., and Babin, M.: Faster Atlantic Currents Drive Poleward Expansion of Temperate Phytoplankton in the Arctic Ocean, *Nature Communications*, 11, 1705, <https://doi.org/10.1038/s41467-020-15485-5>, 2020.
- Pavlov, A. K., Tverberg, V., Ivanov, B. V., Nilsen, F., Falk-Petersen, S., and Granskog, M. A.: Warming of Atlantic Water in Two West Spitsbergen Fjords over the Last Century (1912–2009), *Polar Research*, 32, 1–14, <https://doi.org/10.3402/polar.v32i0.11206>, 2013.
- 650 Percival, D. B. and Walden, A. T.: *Spectral Analysis for Physical Applications*, Cambridge University Press, ISBN 978-0-521-35532-2, <https://doi.org/10.1017/CBO9780511622762>, 1993.
- Polyakov, I. V., Pnyushkov, A. V., Alkire, M. B., Ashik, I. M., Baumann, T. M., Carmack, E. C., Goszczko, I., Guthrie, J., Ivanov, V. V., Kanzow, T., Krishfield, R., Kwok, R., Sundfjord, A., Morison, J., Rember, R., and Yulin, A.: Greater Role for Atlantic Inflows on Sea-Ice Loss in the Eurasian Basin of the Arctic Ocean, *Science*, 356, 285–291, <https://doi.org/10.1126/science.aai8204>, 2017.
- 655 Polyakov, I. V., Ingvaldsen, R. B., Pnyushkov, A. V., Bhatt, U. S., Francis, J. A., Janout, M., Kwok, R., and Skagseth, Ø.: Fluctuating Atlantic Inflows Modulate Arctic Atlantification, *Science*, 381, 972–979, <https://doi.org/10.1126/science.adh5158>, 2023.

- Quadfasel, D., Rudelst, B., and Kurz, K.: Outflow of Dense Water from a Svalbard Fjord into the Fram Strait, *Deep-Sea Research*, 35, 1143–1150, 1988.
- 660 Renner, A. and Sundfjord, A.: Mooring Service Cruise 2021: Cruise Report, The Nansen Legacy Report Series, <https://doi.org/10.7557/nlrs.6461>, 2022.
- Rieke, O., Årthun, M., and Dörr, J. S.: Rapid Sea Ice Changes in the Future Barents Sea, *The Cryosphere*, 17, 1445–1456, <https://doi.org/10.5194/tc-17-1445-2023>, 2023.
- Rudels, B., Jones, E. P., Anderson, L. G., and Kattner, G.: On the Intermediate Depth Waters of the Arctic Ocean, in: *The Polar Oceans and Their Role in Shaping the Global Environment*, pp. 33–46, American Geophysical Union (AGU), ISBN 978-1-118-66388-2, <https://doi.org/10.1029/GM085p0033>, 1994.
- 665 Rudels, B., Schauer, U., Björk, G., Korhonen, M., Pisarev, S., Rabe, B., and Wisotzki, A.: Observations of Water Masses and Circulation with Focus on the Eurasian Basin of the Arctic Ocean from the 1990s to the Late 2000s, *Ocean Science*, 9, 147–169, <https://doi.org/10.5194/os-9-147-2013>, 2013.
- 670 Schauer, U.: The Release of Brine-Enriched Shelf Water from Storfjord into the Norwegian Sea, *Journal of Geophysical Research: Oceans*, 100, 16 015–16 028, <https://doi.org/10.1029/95JC01184>, 1995.
- Schauer, U., Muench, R. D., Rudels, B., and Timokhov, L.: Impact of Eastern Arctic Shelf Waters on the Nansen Basin Intermediate Layers, *Journal of Geophysical Research: Oceans*, 102, 3371–3382, <https://doi.org/10.1029/96JC03366>, 1997.
- Schauer, U., Loeng, H., Rudels, B., Ozhigin, V. K., and Dieck, W.: Atlantic Water Flow through the Barents and Kara Seas, *Deep Sea Research Part I: Oceanographic Research Papers*, 49, 2281–2298, [https://doi.org/10.1016/S0967-0637\(02\)00125-5](https://doi.org/10.1016/S0967-0637(02)00125-5), 2002.
- 675 Shi, J., Luo, B., Luo, D., Yao, Y., Gong, T., and Liu, Y.: Differing Roles of North Atlantic Oceanic and Atmospheric Transports in the Winter Eurasian Arctic Sea-Ice Interannual-to-Decadal Variability, *npj Climate and Atmospheric Science*, 7, 1–13, <https://doi.org/10.1038/s41612-024-00605-5>, 2024.
- Shu, Q., Wang, Q., Song, Z., and Qiao, F.: The Poleward Enhanced Arctic Ocean Cooling Machine in a Warming Climate, *Nature Communications*, 12, 2966, <https://doi.org/10.1038/s41467-021-23321-7>, 2021.
- 680 Skagseth, Ø., Eldevik, T., Årthun, M., Asbjørnsen, H., Lien, V. S., and Smedsrud, L. H.: Reduced Efficiency of the Barents Sea Cooling Machine, *Nature Climate Change*, 10, 661–666, <https://doi.org/10.1038/s41558-020-0772-6>, 2020.
- Skogseth, R., Haugan, P. M., and Haarpaintner, J.: Ice and Brine Production in Storfjorden from Four Winters of Satellite and in Situ Observations and Modeling, *Journal of Geophysical Research C: Oceans*, 109, 1–15, <https://doi.org/10.1029/2004JC002384>, 2004.
- 685 Skogseth, R., Ellingsen, P., Berge, J., Cottier, F. R., Falk-Petersen, S., Ivanov, B. V., Nilsen, F., Søreide, J. E., and Vader, A.: UNIS Hydrographic Database, <https://doi.org/10.21334/unis-hydrography>, 2019.
- Skogseth, R., Olivier, L. L., Nilsen, F., Falck, E., Fraser, N. J., Tverberg, V., Ledang, A. B., Vader, A., Jonassen, M. O., Søreide, J., Cottier, F., Berge, J., Ivanov, B. V., and Falk-Petersen, S.: Variability and Decadal Trends in the Isfjorden (Svalbard) Ocean Climate and Circulation – An Indicator for Climate Change in the European Arctic, *Progress in Oceanography*, 187, 102394, <https://doi.org/10.1016/j.pocean.2020.102394>, 2020.
- 690 Slepian, D.: Prolate Spheroidal Wave Functions, Fourier Analysis, and Uncertainty — V: The Discrete Case, *The Bell System Technical Journal*, 57, 1371–1430, <https://doi.org/10.1002/j.1538-7305.1978.tb02104.x>, 1978.
- Smedsrud, L. H., Esau, I., Ingvaldsen, R. B., Eldevik, T., Haugan, P. M., Li, C., Lien, V. S., Olsen, A., Omar, A. M., Risebrobakken, B., Sandø, A. B., Semenov, V. A., and Sorokina, S. A.: The Role of the Barents Sea in the Arctic Climate System, *Reviews of Geophysics*, 51, 415–449, <https://doi.org/10.1002/rog.20017>, 2013.
- 695

- Smedsrud, L. H., Muilwijk, M., Brakstad, A., Madonna, E., Lauvset, S. K., Spensberger, C., Born, A., Eldevik, T., Drange, H., Jeansson, E., Li, C., Olsen, A., Skagseth, Ø., Slater, D. A., Straneo, F., Våge, K., and Årthun, M.: Nordic Seas Heat Loss, Atlantic Inflow, and Arctic Sea Ice Cover Over the Last Century, *Reviews of Geophysics*, 60, e2020RG000 725, <https://doi.org/10.1029/2020RG000725>, 2022.
- 700 Strzelewicz, A., Przyborska, A., and Walczowski, W.: Increased Presence of Atlantic Water on the Shelf South-West of Spitsbergen with Implications for the Arctic Fjord Hornsund, *Progress in Oceanography*, 200, 102 714, <https://doi.org/10.1016/j.pocean.2021.102714>, 2022.
- Sundfjord, A.: CTD Data from Nansen Legacy Cruise - Mooring Service Cruise 2019, <https://doi.org/10.21335/NMDC-2135074338>, 2022.
- Sundfjord, A.: Nansen Legacy Cruises - Mooring Cruise 2021, <https://doi.org/10.21335/NMDC-499497542>, 2023.
- Sundfjord, A. and Renner, A.: Mooring Service Cruise 2019: Cruise Report, The Nansen Legacy Report Series, <https://doi.org/10.7557/nlrs.5797>, 2021.
- 705 Sundfjord, A., Assmann, K. M., Lundesgaard, Ø., Renner, A. H. H., Lind, S., and Ingvaldsen, R. B.: Suggested Water Mass Definitions for the Central and Northern Barents Sea, and the Adjacent Nansen Basin: Workshop Report, 8, <https://doi.org/10.7557/nlrs.5707>, 2020.
- Thomson, D.: Spectrum Estimation and Harmonic Analysis, *Proceedings of the IEEE*, 70, 1055–1096, <https://doi.org/10.1109/PROC.1982.12433>, 1982.
- Tverberg, V., Skogseth, R., Cottier, F., Sundfjord, A., Walczowski, W., Inall, M. E., Falck, E., Pavlova, O., and Nilsen, F.: The Kongsfjorden Transect: Seasonal and Inter-annual Variability in Hydrography, in: *The Ecosystem of Kongsfjorden, Svalbard*, edited by Hop, H. and Wiencke, C., *Advances in Polar Ecology*, pp. 49–104, Springer International Publishing, Cham, ISBN 978-3-319-46425-1, [https://doi.org/10.1007/978-3-319-46425-1\\_3](https://doi.org/10.1007/978-3-319-46425-1_3), 2019.
- 710 Vihtakari, M., Sundfjord, A., and de Steur, L.: Barents Sea Ocean-Current Arrows Modified from Eriksen et al. (2018), 2019.
- Vinje, T., Jensen, H., Johnsen, A. S., Løset, S., Hamran, S. E., Løvaas, S. M., and Erlingson, B.: IDAP-89 R/V Lance Deployment. Vol. 2. Field Observations and Analysis, Tech. rep., Norwegian Polar Institute/SINTEF NHL, Oslo/Trondheim, 1989.
- 715 Vivier, F., Lourenço, A., Michel, E., Skogseth, R., Rousset, C., Lansard, B., Bouruet-Aubertot, P., Boutin, J., Bombled, B., Cuypers, Y., Crispi, O., Dausse, D., Le Goff, H., Madec, G., Vancoppenolle, M., Van der Linden, F., and Waelbroeck, C.: Summer Hydrography and Circulation in Storfjorden, Svalbard, Following a Record Low Winter Sea-Ice Extent in the Barents Sea, *Journal of Geophysical Research: Oceans*, 128, e2022JC018 648, <https://doi.org/10.1029/2022JC018648>, 2023.
- 720 Wickström, S., Jonassen, M. O., Vihma, T., and Uotila, P.: Trends in Cyclones in the High-Latitude North Atlantic during 1979–2016, *Quarterly Journal of the Royal Meteorological Society*, 146, 762–779, <https://doi.org/10.1002/qj.3707>, 2020.
- Wold, A., Hop, H., Svensen, C., Søreide, J. E., Assmann, K. M., Ormanczyk, M., and Kwasniewski, S.: Atlantification Influences Zooplankton Communities Seasonally in the Northern Barents Sea and Arctic Ocean, *Progress in Oceanography*, 219, 103 133, <https://doi.org/10.1016/j.pocean.2023.103133>, 2023.